The Astrophysical Journal, 786:78 (22pp), 2014 May 10 doi:10.1088/0004-637X/786/2/78

WIDE-FIELD *HUBBLE SPACE TELESCOPE* OBSERVATIONS OF THE GLOBULAR CLUSTER SYSTEM IN NGC 1399*

Thomas H. Puzia[1,2], Maurizio Paolillo[3,4,5], Paul Goudfrooij[6], Thomas J. Maccarone[7], Giuseppina Fabbiano[8], and Lorella Angelini[9]
[1] Institute of Astrophysics, Pontificia Universidad Católica de Chile, Avenida Vicuña Mackenna 4860, Macul, 7820436, Santiago, Chile; tpuzia@astro.puc.cl
[2] National Research Council Canada, Herzberg Institute of Astrophysics, 5071 West Saanich Road, Victoria, BC V9E 2E7, Canada
[3] Department of Physical Sciences, University of Napoli Federico II, via Cinthia 9, I-80126 Napoli, Italy
[4] INFN-Napoli Unit, Department of Physical Sciences, via Cinthia 9, I-80126 Napoli, Italy
[5] Agenzia Spaziale Italiana Science Data Center, Via del Politecnico snc, I-00133 Roma, Italy
[6] Space Telescope Science Institute, 3700 San Martin Drive, Baltimore, MD 21218, USA
[7] Texas Tech University, Physics Department, Box 41051, Lubbock, TX 79409, USA
[8] Harvard-Smithsonian Center for Astrophysics, 60 Garden Street, Cambridge, MA 02138, USA
[9] Laboratory for X-Ray Astrophysics, NASA Goddard Space Flight Center, Greenbelt, MD 20771, USA
Received 2013 August 21; accepted 2014 February 25; published 2014 April 17

ABSTRACT

We present a comprehensive high spatial resolution imaging study of globular clusters (GCs) in NGC 1399, the central giant elliptical cD galaxy in the Fornax galaxy cluster, conducted with the Advanced Camera for Surveys (ACS) aboard the *Hubble Space Telescope* (*HST*). Using a novel technique to construct drizzled point-spread function libraries for HST/ACS data, we accurately determine the fidelity of GC structural parameter measurements from detailed artificial star cluster experiments and show the superior robustness of the GC half-light radius, r_h, compared with other GC structural parameters, such as King core and tidal radius. The measurement of r_h for the major fraction of the NGC 1399 GC system reveals a trend of increasing r_h versus galactocentric distance, $R_{\rm gal}$, out to about 10 kpc and a flat relation beyond. This trend is very similar for blue and red GCs, which are found to have a mean size ratio of $r_{\rm h,red}/r_{\rm h,blue} = 0.82 \pm 0.11$ at all galactocentric radii from the core regions of the galaxy out to ∼40 kpc. This suggests that the size difference between blue and red GCs is due to internal mechanisms related to the evolution of their constituent stellar populations. Modeling the mass density profile of NGC 1399 shows that additional external dynamical mechanisms are required to limit the GC size in the galaxy halo regions to $r_h \approx 2$ pc. We suggest that this may be realized by an exotic GC orbit distribution function, an extended dark matter halo, and/or tidal stress induced by the increased stochasticity in the dwarf halo substructure at larger galactocentric distances. We compare our results with the GC r_h distribution functions in various galaxies and find that the fraction of extended GCs with $r_h \geqslant 5$ pc is systematically larger in late-type galaxies compared with GC systems in early-type galaxies. This is likely due to the dynamically more violent evolution of early-type galaxies. We match our GC r_h measurements with radial velocity data from the literature and split the resulting sample at the median r_h value into compact and extended GCs. We find that compact GCs show a significantly smaller line-of-sight velocity dispersion, $\langle\sigma_{\rm cmp}\rangle = 225 \pm 25$ km s^{-1}, than their extended counterparts, $\langle\sigma_{\rm ext}\rangle = 317 \pm 21$ km s^{-1}. Considering the weaker statistical correlation in the GC r_h color and the GC r_h–$R_{\rm gal}$ relations, the more significant GC size–dynamics relation appears to be astrophysically more relevant and hints at the dominant influence of the GC orbit distribution function on the evolution of GC structural parameters.

Key words: galaxies: evolution – galaxies: formation – galaxies: individual (NGC 1399) – galaxies: star clusters: general – globular clusters: general

Online-only material: color figures

1. INTRODUCTION

1.1. Structural Parameters of Extragalactic Globular Clusters

Wide-field studies of massive galaxies provide important benchmarks for comparisons with globular cluster (GC) formation and evolution models as well as GC system assembly in the context of galaxy formation scenarios, not only because they define homogeneous and uniform data sets but also because they simultaneously sample galaxy core and halo regions where various different physical processes affect the GC formation and survivability. In general, GC formation is influenced by small-scale physics that governs star formation and feedback processes (e.g., Murray & Lin 1992; Harris & Pudritz 1994; Elmegreen & Efremov 1997; Hartwick 2009; Murray 2009), while stellar feedback and internal and external dynamical mechanisms determine their early evolution (Gieles & Bastian 2008; Bastian et al. 2008; Fall et al. 2009; Chandar 2009; Elmegreen & Hunter 2010; Mapelli & Bressan 2013) and the latter ultimately determines their fate (e.g., Gnedin & Ostriker 1997; Vesperini & Heggie 1997; Vesperini & Zepf 2003; Chandar et al. 2010; Bekki 2010). The vast dynamical parameter ranges that need to be probed to study the complex interplay of these processes with numerical simulations are still very challenging for today's computers (e.g., Kravtsov & Gnedin 2005; Li et al. 2005; Bournaud et al. 2008; Griffen et al. 2010; Schulman et al. 2012; Greif et al. 2012). One simple approach

* Based on observations with the NASA/ESA *Hubble Space Telescope* obtained at the Space Telescope Science Institute, which is operated by the Association of Universities for Research in Astronomy, Incorporated, under NASA contract NAS5-26555.

to understand the influence of some of these processes on GC formation and evolution is the empirical study of GC structural parameters and their variation as a function of galactocentric distance.

Detailed GC structural parameters, such as core, half-light, and tidal radii, as well as central surface brightness, concentration, ellipticity, etc., were, until the past decade, only accessible within the Local Group (LG) because of the limited spatial resolution of ground-based instrumentation (e.g., King et al. 1968; Illingworth & Illingworth 1976; Kontizas et al. 1982; Elson & Freeman 1985; Elson & Walterbos 1988; Elson 1991, 1992; Crampton et al. 1985; Demers et al. 1990; Trager et al. 1995). The launch of the *Hubble Space Telescope* (*HST*) catapulted this field to a whole new stratum, making vast numbers of GC systems accessible to high spatial resolution studies (Harris et al. 2013). In fact, *HST* still provides our only access to high spatial resolution observations at optical wavelengths. Several pioneering *HST* works quickly reached out with their GC half-light radius measurements beyond the LG as far as the Fornax galaxy cluster at ∼20 Mpc distance (e.g., Elson & Schade 1994; Fusi Pecci et al. 1994; Kundu & Whitmore 1998; Kundu et al. 1999; Puzia et al. 1999, 2000; Zepf et al. 1999). Numerous subsequent studies have used the superior spatial resolution of *HST* and the relatively large field of view (∼202″ × 202″) of the Advanced Camera for Surveys (ACS) to collect large imaging data sets of extragalactic GC systems, the most homogeneous of which was obtained by the ACS Virgo and Fornax Cluster Surveys (ACSVCS and ACSFCS; see Côté et al. 2004 and Jordán et al. 2007, respectively). These observations set the baseline for systematic studies of GC structural parameters in the central regions of early-type cluster galaxies. There was quickly mounting consensus among the early *HST* investigations that the observed central GCs had a rather broad half-light radius distribution with a peak somewhere in the range ∼2–3 pc, which led to the suggestion that this peak value may be used as a geometric distance indicator (e.g., Kundu & Whitmore 2001; Jordán et al. 2005). Another important finding was that the blue GCs are, on average, larger than the red GCs. In particular, within the central regions of galaxies typically observed with *HST*, blue GCs show ∼20% larger mean half-light radii compared to the red GC subpopulation (e.g., Kundu & Whitmore 1998, 2001; Kundu et al. 1999; Puzia et al. 1999, 2000; Zepf et al. 1999; Larsen et al. 2001; Jordán et al. 2005; Spitler et al. 2006; Harris et al. 2006, 2010; Harris 2009; Blom et al. 2012; Goudfrooij 2012).

However, one major limitation of most previous *HST* studies, targeting extragalactic GC systems such as the ACS Virgo and Fornax cluster surveys, was their limited field of view, using only one *HST*/ACS pointing per galaxy. Because of this, these *HST* studies focused on the core regions of elliptical galaxies covering the inner few kiloparsecs (i.e., $\lesssim 1 R_{\rm eff}$). The outer parts of rich GC systems in central cluster galaxies have so far been missed and mainly observed with ground-based instrumentation at much lower spatial resolutions (e.g., Rhode & Zepf 2001, 2004; Rhode et al. 2007). The only other ground-based study featuring a wide field of view and high spatial resolution was performed by Gómez & Woodley (2007) using Magellan/IMACS under exceptional ∼0.″5 average seeing conditions to measure half-light radii of 364 radial-velocity-confirmed GCs in NGC 5128 (S0/E) out to $\sim 8 R_{\rm eff}$ of the spheroid light, and it found no significant correlation between GC half-light radius and projected galactocentric distance, i.e., $r_h \propto R^0$, outside $\sim 1 R_{\rm eff}$. However, Gómez & Woodley reported that at $\lesssim 1 R_{\rm eff}$ the red GCs show a steeper r_h–R relation and, on average, 30% smaller sizes than blue GCs.

Other studies using more than single-pointing *HST* observations conducted GC half-light radius measurements in NGC 4594 (Sa) out to about $6 R_{\rm eff}$ of the bulge component (Spitler et al. 2006; Harris et al. 2010, 658 GC candidates), in NGC 4365 (E) out to $\sim 2.4 R_{\rm eff}$ (Blom et al. 2012, 659 GC candidates) as well as in NGC 4278 (E1-2) out to $\sim$6–$7 R_{\rm eff}$ of the spheroid light (Usher et al. 2013, 716 GC candidates), and in six giant elliptical galaxies out to $\sim$4–$5 R_{\rm eff}$ of their spheroids (Harris 2009, altogether 3330 GC candidates). In the case of NGC 4594, the inner red GCs are ∼17% smaller than the blue ones, but because of a steeper size–radius relation of the red GC subpopulation, this difference becomes insignificant at galactocentric radii $\gtrsim 2.7 R_{\rm eff}$ of the bulge light. NGC 4365 hosts, on average, ∼32% larger blue GCs compared to their red counterparts and shows a steep size–radius relation, $r_h \propto R^{(0.49\pm0.04)}$, for the entire GC sample, similar to the Milky Way's GC system (van den Bergh et al. 1991). However, Blom et al. do not investigate whether this relation differs between GC subpopulations as a function of projected galactocentric radius. The composite GC system of the six giant ellipticals studied by Harris exhibits a mild relation of the form $r_h \propto R^{0.11}$ and an ∼17% size difference between red and blue GCs that is independent of projected galactocentric radius.

1.2. Astrophysical Implications

In general, the finding of a size difference between blue and red GCs has important astrophysical implications for the understanding of the formation and evolution of GCs and for the usefulness of the peak value of the GC size distribution as geometric distance indicator. Several studies, such as Larsen & Brodie (2003), Jordán (2004), and Harris (2009), put forward models to explain the size difference between blue and red GCs. Inspired by the Milky Way GC system where a shallow relation exists between GC half-light radius and the three-dimensional galactocentric distance, $r_h \propto R_{\rm 3D}^{0.5}$ (van den Bergh et al. 1991), Larsen & Brodie suggested that the GC size difference between red and blue GCs in massive ellipticals could be due to the difference in their spatial distribution functions. Typically, the red GC subpopulation would be more centrally concentrated than its blue counterpart and therefore, on average, smaller, being tidally more truncated by the stronger host galaxy potential. However, Webb et al. (2012a) have shown in detailed numerical simulations that the observed GC size difference is unlikely due to projection effects alone. In contrast to this external effect, two alternative internal effects were put forward. First, Jordán (2004) suggested that the combined effect of mass segregation and shorter stellar lifetimes of more metal-rich stars at a given mass may explain the GC size difference. This was strictly valid under the assumption that the GC half-mass radius distribution would be independent of metallicity and that metal-poor and metal-rich GCs were of the same age, which may be at odds with observations (e.g., Puzia et al. 2002; Marín-Franch et al. 2009; Goudfrooij 2012). This scenario was further developed by Sippel et al. (2012) and Schulman et al. (2012) in direct-integration *N*-body simulations of young, low-mass clusters with and without initial mass segregation, the absence of which was found to enhance the GC size difference. Downing (2012) performed Monte Carlo *N*-body simulations of massive star clusters and found that significant numbers of massive stellar remnants, i.e., single and binary black holes, would boost this GC size difference. Second, Harris (2009) suggested that

more metal-rich proto-GC clouds could cool more efficiently and therefore collapse into a more concentrated quasi-equilibrium state before forming stars than clusters formed from low-metallicity gas. Any of these three scenarios comes with limiting assumptions and is likely not the single cause for the measured GC size difference as the variety of results described above indicates.

To provide a larger and statistically robust data set to constrain GC sizes as a function of galactocentric radius, we embarked on a wide-field observing campaign covering a large area with an *HST*/ACS mosaic out to several effective radii ($>5R_{\rm eff}$) of the diffuse spheroid light around NGC 1399, the central galaxy in the Fornax galaxy cluster that hosts one of the richest ($\gtrsim$6000 GCs; specific frequency[10] $S_N \approx 5$) and most extended GC systems in the nearby universe (Dirsch et al. 2003; Faifer et al. 2004; Bassino et al. 2006). A significant part of the outer-halo GC system of NGC 1399 is located hundreds of kiloparsecs away from its host and is probing the transition regime between galaxy and cluster potential (Ferguson & Sandage 1989). At the same time, the formation efficiencies of these outer-halo blue GCs appear to be higher than those of the inner red GCs; S_N(red) $\approx$ 3 while S_N(blue) $\approx$ 14 (Forte et al. 2005). Spectroscopic radial velocity studies of hundreds of GCs established a very complex multi-component system with the blue GCs being kinematically distinct from the red GC subpopulation, the latter of which shows dynamics similar to that of the host galaxy diffuse stellar component. The blue GCs, on the other hand, seem to have been partly accreted from satellite galaxies (Schuberth et al. 2010). It is this large auxiliary kinematic data set that makes the GC system of NGC 1399 an ideal target for a wide-field, high spatial resolution study with *HST*/ACS (in comparison to M87, e.g., Peng et al. 2009; Madrid et al. 2009) as several hundreds of member stellar systems are robustly separated from the fore- and background in radial velocity space.

In our previous works, we used the data set from this paper to study the low-mass X-ray binary (LMXB) population and the correlation of their properties with GC structural parameters (Paolillo et al. 2011; D'Ago et al. 2014), as well as the GC selection techniques based on neural algorithms (Brescia et al. 2012). Here we focus on the properties of the GC system itself. Our present paper is organized as follows: in Section 2 we present the *HST*/ACS observations and discuss the details of subpixel dithering; Section 3 includes a description of the preliminary photometry that enters our structural parameter fitting code, which is introduced and thoroughly tested in Section 4. We present our results in Section 5, where we show the large-scale variations of GC structural parameters within NGC 1399. We discuss the implications in Section 6 and conclude this work in Section 7.

2. OBSERVATIONS

2.1. Field Coverage and Orientation

All observations were taken as part of the program GO-10129 (PI: Puzia) with the ACS (Ford et al. 2003) on board the *HST* in 2004 November and 2005 April. The pointings were arranged in a 3 × 3 ACS mosaic with a few arcseconds overlap between the individual tiles, as illustrated in Figure 1. To maximize common-field coverage with other imaging and spectroscopy observations (i.e., *Chandra* X-ray imaging (see Paolillo et al. 2011) and Very Large Telescope (VLT) ground-based spectroscopy), the entire mosaic is rotated with a position angle of about −30° with respect to the meridian and centered on the coordinates: R.A. (J2000) = $03^{\rm h}38^{\rm m}28\overset{\rm s}{.}62$ and decl. (J2000) = $-35°28'18\overset{''}{.}9$. Because of scheduling constraints the north, northeast, and northwest tiles were observed with a position angle of $-30\overset{\circ}{.}467$, while the other six tiles were taken at a position angle of $149\overset{\circ}{.}552$. The full mosaic covers roughly $10' \times 10'$ arcmin and extends out to a maximum projected galactocentric distance of $8\overset{'}{.}76$ or 51.3 ± 1.0 kpc with respect to NGC 1399 (adopting the distance D = 20.13 ± 0.4 Mpc; see Dunn & Jerjen 2006, see also Blakeslee et al. 2009). This corresponds to a projected coverage of ∼5.2 effective radii of the NGC 1399 diffuse galaxy light (de Vaucouleurs et al. 1991) and ∼4.9 core radii of the globular cluster system density profile[11] (Schuberth et al. 2010).

Table 1
Parameters of the Utilized Dither Pattern

Parameter	Value
Pattern type	ACS-WFC-DITHER-BOX
Primary pattern shape	PARALLELOGRAM
Pattern purpose	DITHER
Number of points	4
Point spacing	$0\overset{''}{.}285$
Line spacing	$0\overset{''}{.}285$
Coordinate frame	POS-TARG
Pattern orient	30.155 deg
Angle between sides	145.82 deg
Center pattern	NO

Our filter choice considerations included the optimization of throughput, detector sensitivity, high spatial resolution, and a well-defined transformation to a standard photometric system. The filter that optimally balances these effects is F606W and was used for all our exposures. The ACS Wide-Field Channel (WFC) spatial sampling of the point-spread function (PSF) is subcritical at the wavelength of our observations (F606W ≈ 4600–7200 Å). If not accounted for, this would introduce aliasing artifacts and significantly degrade the spatial information in the final images, thus hampering the measurement of globular cluster structural parameters at the distance of Fornax. Each tile was therefore observed in a single orbit in four dithered subexposures of 527 s to allow subpixel resampling (see below), yielding a total integration time of 2108 s.

2.2. Data Reduction and Image Combination

The basic data reduction of each ACS/WFC dither set was performed by the ACS data pipeline CALACS (Hack et al. 2003). The reduction steps included subtraction of master bias and master dark images, correction for flat-field and gain variations, and elimination of bad pixels.

For the dithered observations we adopted a slightly modified Hubble Ultra-Deep Field (HUDF) dither pattern, for which the dither parameters are provided for reference in Table 1. Note that

[10] The specific frequency of a GC system is defined as twice the number of GCs brighter than the turnover luminosity of the GC luminosity function, given by $N_{\rm GC}$, relative to the absolute V-band luminosity of the host galaxy, M_V, which is normalized to −15 mag. This quantity is defined as the specific frequency of a GC system $S_N = N_{\rm GC}10^{0.4(M_V+15)}$; see also Georgiev et al. (2010) and Harris et al. (2013) for other GC system scaling relations.

[11] Schuberth et al. (2010) approximate the radial GC system number density distribution with a cored power-law profile of the form $N(R) \propto ((R/R_0)^2+1)^{-\alpha}$, where the core radius is $R_0 = 1\overset{'}{.}74 \pm 0\overset{'}{.}27$ and the power-law exponent $\alpha = 0.84 \pm 0.02$.

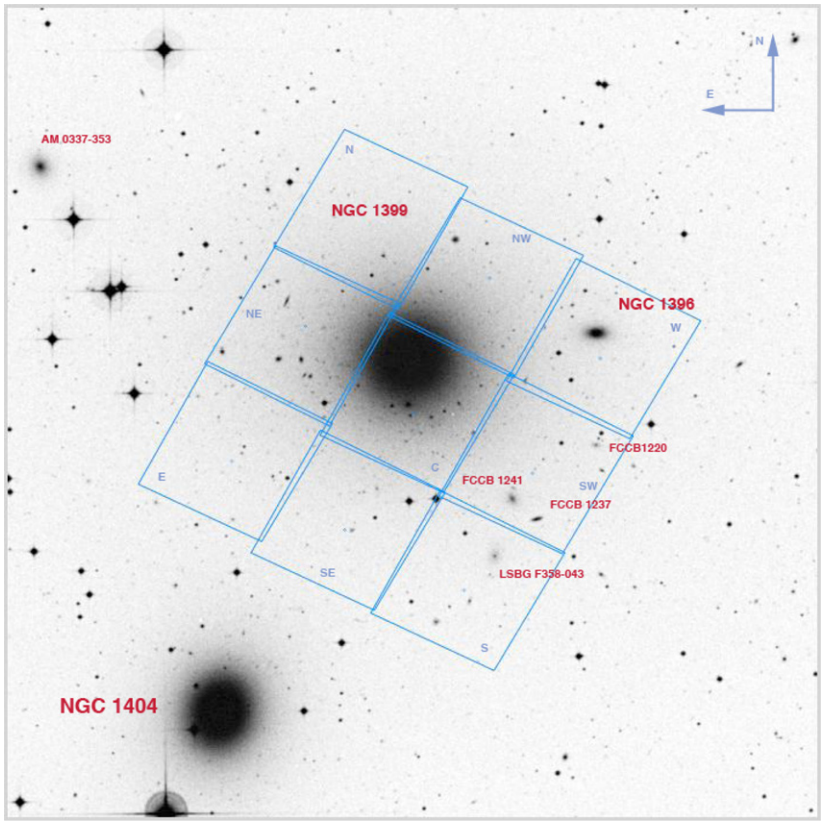

Figure 1. Illustration of the 3 × 3 mosaic of our ACS observations overplotted on a DSS-2 image. Individual tiles and the main galaxies in the field are labeled. The orientation of the image, which measures 20′ × 20′, is indicated in the upper right corner.

(A color version of this figure is available in the online journal.)

this dither pattern is not designed to cross the ACS interchip gap but to maximize the subpixel shift integrity over the full ACS/WFC field of view. In its shape it follows the UDF dither pattern with a 67% larger step size.

Each set of four dithered frames was combined into a single image using the MultiDrizzle routine version 2.7.0 (Koekemoer et al. 2003). The software takes care of correcting the geometric field distortions that affect individual ACS exposures and projects all dithered images onto a common grid in which the rectified frames are averaged. The averaged image is then "blotted" back into each distorted frame to identify and clean cosmic rays and bad pixels and columns by means of comparison of input versus averaged image (see Fruchter & Hook 2002). No background subtraction was performed at this stage of data processing. The main background contribution in our fields is due to the NGC 1399 diffuse light and is correctly accounted for in the following structural profile analysis (see Section 4.2).

Similar to the GOODS and UDF data sets, we use the Gaussian drizzle kernel and set the pixel scale to 0.″03 pixel^{-1} on the final combined images. This provides a super-Nyquist sampling of the PSF with a FWHM of ∼0.″08 at 6000 Å (see Beckwith et al. 2006). Rhodes et al. (2007) find that this combination of Gaussian drizzle kernel and 0.″03 pixel^{-1} output pixel scale gives minimal aliasing in the final images. Jee et al. (2007) argue that a Lanczos drizzle kernel with a 0.″05 pixel^{-1} output scale reduces the PSF width by ∼3% compared to the Gaussian kernel at the expense that the Lanczos kernel introduces "cosmetic artifacts in the regions where flux gradients change abruptly" (Jee et al. 2007, p. 1411). Since most of our target GCs are likely to have structural parameters at the resolution limit of *HST* we are expecting strong varying profile gradients for the most compact objects. We find that noise correlation between neighboring pixels produces moiré patterns in the vicinity of bright objects and strong gradients (see Rhodes et al. 2007), but this affects only a few blended sources in our data set. After these considerations and careful visual inspection of the drizzled images, we therefore decide to use the Gaussian drizzle kernel with PIXFRAC = 0.8 in the subsequent analysis. The combined field is illustrated in Figure 2 and has an effective field of view of 99.053 arcmin^2.

Using the MultiDrizzle software, we also produce weight and error maps representing the final error budget for each pixel, which account for all uncertainties in the reduction process, including bias, flat-field, drizzling, and aliasing effects. These weight and error maps enter the photometry and structural parameter analysis. We note that the high spatial resolution of our drizzled images safeguards them from crowding effects, even in the central regions of NGC 1399, and reveals in every pointing a wealth of detail in object morphology, as illustrated in Figure 3.

3. THE PHOTOMETRIC INPUT CATALOG

3.1. Aperture Photometry and Astrometry

To obtain a rough estimate of the total magnitudes of all detected sources, we perform aperture photometry with the SExtractor package (Bertin & Arnouts 1996) and measure instrumental magnitudes in apertures of successively growing diameter, i.e., photometric growth curve analysis. We use the asymptotic limit of these curves to compute mean photometric corrections from finite aperture sizes to "infinity." Our

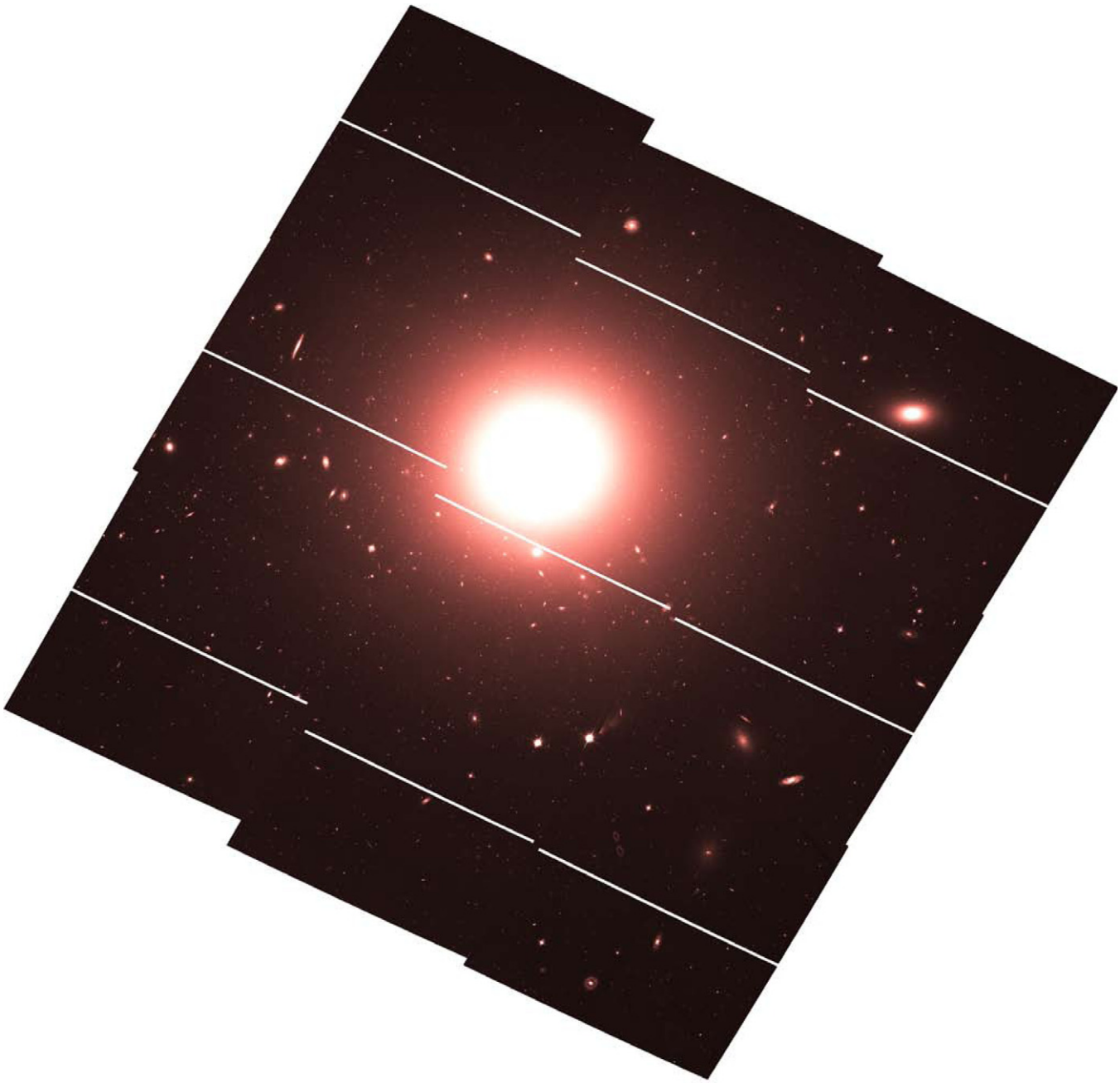

Figure 2. Composite field of view of the combined 3 × 3 ACS mosaic roughly centered on NGC 1399. The effective area of the observed sky is 99.053 arcmin^2, and it covers ∼4.9 core radii of the globular cluster system in NGC 1399 (Schuberth et al. 2010) and ∼5.7 effective radii of the NGC 1399 diffuse galaxy light (de Vaucouleurs et al. 1991). The dimensions of this field are 13.′78 in R.A. and 13.′75 in decl. The white lines are the ACS/WFC interchip gaps, which were not covered by our dither pattern. North is up; east is to the left.

(A color version of this figure is available in the online journal.)

tests show that an aperture with 0.″24 radius maximizes the signal-to-noise ratio (S/N) of the final photometry. Leaving out saturated objects and spurious detections, we obtain a mean aperture correction for this optimal aperture size to an "infinite" aperture radius of $\langle\Delta_{\rm F606W}\rangle = -0.14$ mag (with a standard deviation $\sigma = 0.22$ mag). We also measure the mean photometric correction from the standard 0.″5 aperture radius to infinity $\langle\Delta_{\rm F606W}\rangle = -0.07$ mag (with a standard deviation $\sigma = 0.14$ mag), which compares well with the suggested value from Sirianni et al. (2005) of $\langle\Delta_{\rm F606W}\rangle = -0.088$ mag.

We follow the prescriptions of Sirianni et al. (2005) to calibrate our F606W infinite-aperture magnitudes m_i to the broadband V filter in the VEGAMAG filter system. We include second-order color terms from the synthetic model of Sirianni et al. that are applicable for the color range $V - I > 0.4$ mag and obtain the final photometric calibration equation

$$V_{\rm F606W} = m_i + 26.331 + 0.340\,(V - I) - 0.038\,(V - I)^2, \quad (1)$$

where we assume a mean $V - I = 0.95 \pm 0.1$ mag for our globular cluster candidates (see, e.g., Peng et al. 2006). All frames have a minimum background flux level of $\sim 40e^-$ per subintegration, which would correspond to a charge transfer efficiency (CTE) correction of the order of $\lesssim$0.02 mag across each WFC chip (Riess & Mack 2004;

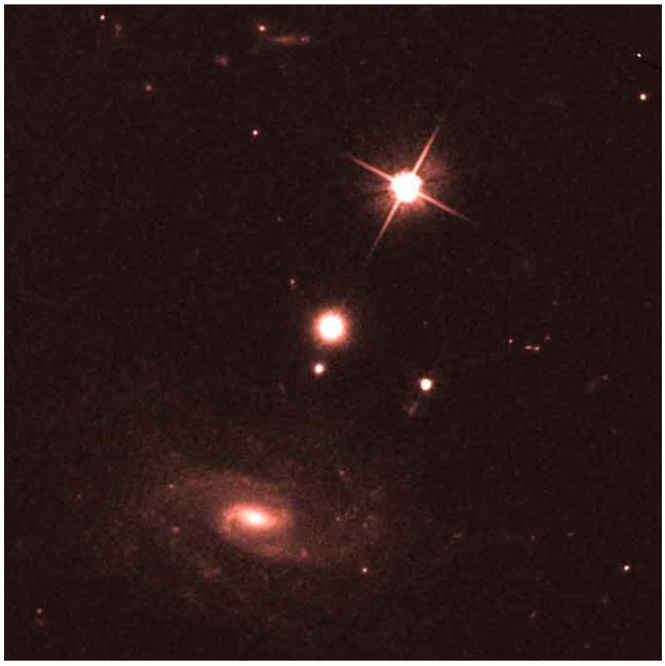

Figure 3. This approximately 35″ × 35″ image cutout is an illustration of the data quality of our drizzled *HST*/ACS mosaic frames, featuring a representative region with a bright foreground star, several resolved compact stellar systems in NGC 1399, a background spiral galaxy with its own disk star cluster system, and many faint background sources. North is up; east is to the left.

(A color version of this figure is available in the online journal.)

Kozhurina-Platais et al. 2007). Since the average background level in all ACS mosaic tiles is higher than the minimum background flux, we do not correct for this negligible photometric offset. The Galactic foreground extinction in the direction of NGC 1399 is $E(B-V) = 0.013$ mag (Schlegel et al. 1998; Schlafly & Finkbeiner 2011), which translates into $A_{\rm F606W} = 0.038$ mag using the Schlegel et al. (1998) reddening curve. The total uncertainty of the photometric calibration in Equation (1) formally amounts to ∼0.089 mag. However, when we consider the small CTE corrections, a color mismatch of ∼0.1 mag in Equation (1) for GCs with extreme $V-I$ colors, and potential differential reddening of ∼0.05 mag across the ACS mosaic field, we estimate that our final photometry is accurate to $\Delta V_{\rm F606W} \approx 0.1$ mag. It is important to note that at this point we are not concerned with achieving photometry of the highest possible quality but providing first-guess input catalogs for our profile fitting routine.

To be able to match source detections taken with other telescopes, we compute an absolute astrometric solution for each of the nine ACS tiles. We select 40 bright unsaturated stars distributed homogeneously over the entire mosaic and match their positions with those of stars from the USNO-B1 catalog[12] (Monet et al. 2003) to obtain the world coordinate solution (WCS) for each tile. The final WCS accuracy across the entire mosaic is ∼0.″2.

3.2. Object Classification

In the following we describe the object detection and classification schemes that were used to define a photometrically selected globular cluster candidate (GCC) sample for which we later measure structural parameters (see Section 4). On the drizzled stack images we measure object coordinates, the background level, Kron radius,[13] isophotal area, FWHM, ellipticity, position angle, and the SExtractor quality flag parameter of each detection that had at least 20 pixels approximately 1.6σ above the background noise, corresponding to S/N ≈ 6. The error images, produced during the drizzle procedure, were used as weight maps in the detection process to account for the varying NGC 1399 surface brightness.

Rather than trying to find the optimal source parameters to select high-probability GCCs, we adjust our classification parameters to reject clearly extended and/or amorphous background objects and image artifacts. Visual inspection of the individual frames shows that a very reliable rejection of clearly extended background sources and image artifacts is provided by the following parameter cuts: $\Delta V_{\rm F606W} < 0.1$ mag, Kron radius $r_k < 0.''21$, FWHM $< 0.''75$, ellipticity $(1 - b/a) < 0.8$ (see Figure 4). The ellipticity criteria are based on Local Group GCs (see also Jordán et al. 2009), while the FWHM cut is set at about ∼10 times the one of the stellar PSF, and in Brescia et al. (2012) we showed that using more restrictive criteria may result in losing extended GCs, such as ωCen. The photometric uncertainty cut is to ensure reliable fitting (approximately equivalent to Paolillo et al. 2011) since at less conservative cuts the galaxy background begins to dominate (see Section 4.4.4 and Figure 5). Additional criteria are the SExtractor flag parameter set to <4, which excludes objects with incomplete and/or corrupted photometry apertures that are very close to the frame edges, and the total isophotal area limit of $\lesssim$6000 pixel,[14] which eliminates particularly extended galaxies and saturated foreground stars.

The final input catalog contains 6634 sources. We show the $V_{\rm F606W}$ luminosity function of all detected and selected objects in Figure 5. We point out that the above selection criteria serve only as preparation of our sample for the next step of the analysis, i.e., the profile fitting routine, and are intended to minimize human interaction during the fitting process. In particular, they do not affect our final results.

3.3. Estimating the Background Galaxy Contribution

We estimate the contribution of the background galaxy population to the luminosity distribution of our input catalog (see Figure 5) by applying the exact same photometry procedure to the F606W observations that were obtained as part of the HUDF program (Beckwith et al. 2006). The HUDF observations were conducted in 112 subexposures spread over 56 orbits with a total integration time of 135,320 s and give us excellent access to high-quality background galaxy photometry. We obtained the drizzled HUDF image and the corresponding weight map from the Hubble Data Archive as reduced higher-level science products,[15] which were produced with virtually identical multidrizzle parameters compared with our procedure (see Section 2.2). To avoid unnecessary profile fitting of the many extended and amorphous sources in the HUDF, we use SExtractor to measure their MAG_BEST magnitudes, corrected for Galactic foreground extinction $E_{(B-V)} = 0.008$ mag, and plot the corresponding luminosity function in Figure 5. Since the final HUDF frame covers 11 arcmin^2 with a spatial

[12] http://tdc-www.harvard.edu/software/catalogs/ub1.html

[13] The Kron radius is defined as $r_k = \sum r\,I(r) / \sum I(r)$. A circular aperture of radius $2r_k$ encloses ⩾90% of an object's flux independent of its magnitude (Kron 1980).

[14] We note that in Paolillo et al. (2011) and Brescia et al. (2012) the selection criteria were somewhat different, although broadly consistent, as those works had a different objective.

[15] http://archive.stsci.edu/prepds/udf

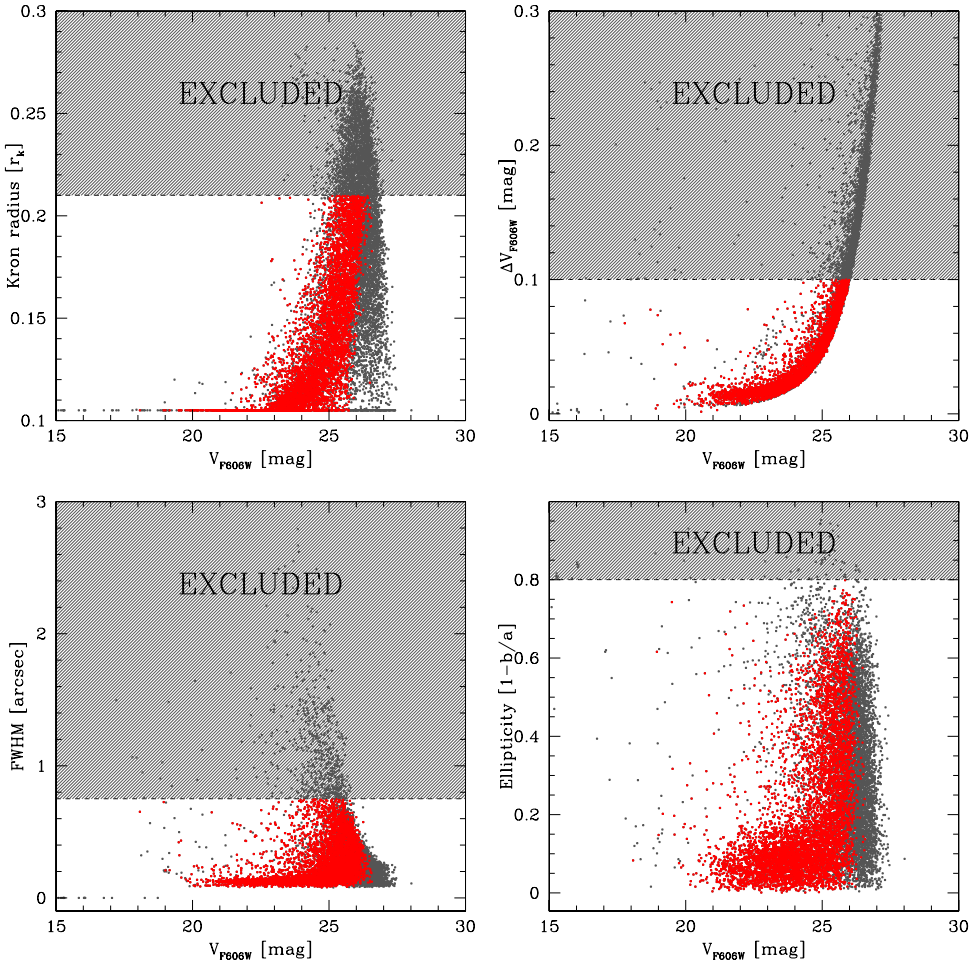

Figure 4. Top panels show the photometric diagnostics (from the top right panel counterclockwise) photometric uncertainty, Kron radius, FWHM, and ellipticity as a function of $V_{\rm F606W}$ magnitude for all detected objects in the ACS mosaic (gray data). The hatched regions indicate objects excluded by the selection cuts that are used to reject extended and/or amorphous background objects and image artifacts. The selected objects (red data) are used as the input sample to measure their structural parameters. See Section 3.2 for details.

(A color version of this figure is available in the online journal.)

sampling of $0\farcs03$ pix^{-1}, we therefore scale the galaxy background number counts by a factor of 9.005 to match the survey area of our ACS mosaic.

The plot shows the remarkable similarity of the faint end of the luminosity distribution of our sample with the background galaxy population, modulo a small difference at faint magnitudes $V_{\rm F606W} \gtrsim 26$ mag, which is likely the manifestation of cosmic variance; for example, there is a variation in the number of background galaxy clusters in our ACS mosaic field. This is consistent with the results of Hilker et al. (1999) and Drinkwater et al. (2000), who find a background galaxy cluster at $z = 0.11$ behind the core of the Fornax galaxy cluster.

4. ANALYSIS

At the distance of Fornax (20.13 ± 0.4 Mpc) 1 arcsec spans 97.6 pc. On our drizzled ACS frames 1 pixel with the angular size of $0\farcs03$ subtends therefore 2.93 pc at the distance of NGC 1399. This is similar to the typical half-light radius for Milky Way globular clusters (Harris 1996). *HST*'s confusion limit, δ, at the pivot wavelength of the F606W filter, $\lambda_p = 606$ nm, can be estimated via $\delta = 1.22\,\lambda_p/D$, where $D = 2.4$ m of the *HST* primary mirror. We obtain $\delta = 6.2$ pc at the distance of Fornax. However, because we are fitting analytical, multiple-component two-dimensional (2D) surface brightness profiles, our nominal spatial resolution is much better than the computed confusion limit. The exact numerical value of the spatial resolution limit is determined through detailed artificial cluster experiments, which are discussed in Section 4.4 in detail.

Observations of the integrated-light profile $\Sigma(\boldsymbol{r})$ of resolved astronomical objects measure their surface brightness variations $\mu(\boldsymbol{r})$ over the 2D spatial extent (r = $\boldsymbol{r}$ for spherically symmetric sources) convolved with the instrumental point-spread function $P(\boldsymbol{r})$ and the detector diffusion kernel $D(\boldsymbol{r})$, plus, in the simplest case, an additive noise term $N(\boldsymbol{r})$:

$$\Sigma(\boldsymbol{r}) = 2\pi \int_{r_1}^{r_2} \{\mu(\boldsymbol{r}) \otimes P(\boldsymbol{r}) \otimes D(\boldsymbol{r}) + N(\boldsymbol{r})\}\, \boldsymbol{r}\, d\boldsymbol{r} \qquad (2)$$

where $\mu(\boldsymbol{r})$ is the sum of the source and background surface brightness $\mu_{\rm s}(\boldsymbol{r}) + \mu_{\rm b}(\boldsymbol{r})$. The access to surface brightness profiles of distant objects (e.g., globular clusters in NGC 1399) is therefore limited by the spatial resolution of the data (i.e., the width of functions $P(\boldsymbol{r})$ and $D(\boldsymbol{r})$), the brightness of the sky (i.e., where $\mu(\boldsymbol{r}) \approx \mu_{\rm b}$), and the noise properties of the data (i.e., $N(\boldsymbol{r})$). Among today's imaging instruments that operate at optical wavelengths, the ideal case of $P(\boldsymbol{r}) \otimes D(\boldsymbol{r}) \rightarrow \delta(\boldsymbol{r})$ and $N(\boldsymbol{r}) \rightarrow 0$ is best approximated by *HST*. In particular, the ACS/WFC camera provides a large field of view ($\sim 202'' \times 202''$) over

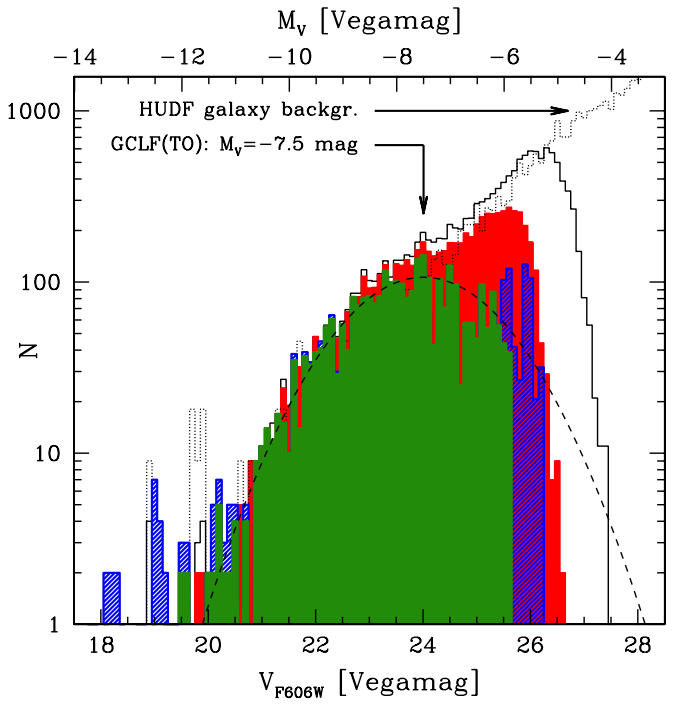

Figure 5. Luminosity distribution of all F606W detections around NGC 1399 in our 3 × 3 ACS mosaic (solid open histogram) and the background galaxy contribution estimated from the HUDF based on the same object detection criteria (dotted open histogram). Our preselected sample that enters the structural parameter measuring routine is shown as a solid red histogram. To illustrate the influence of the background galaxy population on the faint end of our input catalog sample, we statistically subtract the background galaxy distribution (dotted open histogram) from our initial photometric sample (solid open histogram) and show the result as the hatched blue histogram. The corresponding result after filtering with the photometric preselection (see Section 3.2 for details) is shown as the solid green histogram. This is in remarkable agreement with the expected classic GC luminosity function with $M_V(\mathrm{TO}) = -7.5$ mag and $\sigma_{\mathrm{GCLF}} = 1.4$ mag, which is indicated as a dotted curve (e.g., Richtler 2003). The top axis shows absolute magnitudes assuming a distance of $D = 20.13$ Mpc.
(A color version of this figure is available in the online journal.)

which the geometric variations of $P(\boldsymbol{r}) \otimes D(\boldsymbol{r})$ are relatively stable and well understood (Anderson 2005; Jee et al. 2007). An additional major advantage of *HST* observations is the very low sky background with a typical surface brightness $\mu_{\mathrm{b},V} \gtrsim 22.5$ mag arcsec^{-2} (see also the ACS Instrument Handbook[16]).

4.1. King Surface Brightness Profile

The reason for the great success of the King profile in parameterizing the surface brightness profiles of most Galactic globular clusters is their structural homology and is a simple consequence of the fact that virtually all of these systems have ages far in excess of their relaxation times (e.g., King et al. 1968; Illingworth & Illingworth 1976; Da Costa 1979; Kukarkin & Kireeva 1979; Chun et al. 1980; Trager et al. 1995). We note here en passant that this might not be the case for more extended sources (e.g., Misgeld & Hilker 2011). The King profile (King 1962), which is defined as

$$\mu_{\mathrm{K}}(\boldsymbol{r}) = k\left[\left(1+\frac{\boldsymbol{r}^2}{r_c^2}\right)^{-\frac{1}{2}} - \left(1+\frac{r_t^2}{r_c^2}\right)^{-\frac{1}{2}}\right]^2, \qquad (3)$$

[16] http://www.stsci.edu/nst/acs

describes the surface number density in the range $0 \leqslant |\boldsymbol{r}| < r_t$ and is zero for $\boldsymbol{r} \geqslant r_t$. Its shape is governed by the core radius r_c, at which the projected surface density is half the central stellar surface density, which itself is set by the cluster gravitational binding energy ($r_c \approx 3\sigma/\sqrt{4\pi G\rho_o}$ for $r_t/r_c \gg 1$; see, e.g., Binney & Tremaine 1987). If the GC is tidally filling, r_t can be considered the tidal radius; otherwise, r_t marks the limiting radius beyond which the stellar density drops to zero. This is sometimes referred to as the King radius (r_k). The profile is normalized to the central surface brightness by $k = \mu(0)(1 - 1/\sqrt{1 + r_t^2/r_c^2})^{-2}$. The family of King profiles is parameterized by the concentration $c = r_t/r_c$, which is directly proportional to the central potential W_o via $c \simeq 9.12 + (W_o - 4.215)^{3.064}$ for $W_o \leqslant 12$ (King 1966, see also Binney & Tremaine 1987). The basic assumption of this parameterization is a truncated (so-called lowered) Maxwellian phase-space distribution of GC member stars in addition to the premise of orbital isotropy.

It is assumed that the King profile is a valid description of the surface brightness profiles of extragalactic GCs (e.g., Harris et al. 2002, 2010; Sharina et al. 2005; Jordán et al. 2005; Huxor et al. 2005; Gómez et al. 2006; Barmby et al. 2007; McLaughlin et al. 2008; Masters et al. 2010). In other words, we assume a universal homology among globular clusters and adopt the King structural parameters as a sufficient set to describe their light profiles. However, we have to keep in mind that such objects may not be well represented by isotropic, single-mass, isothermal spheres but may be better described by other profiles. McLaughlin & van der Marel (2005) show that other profiles such as the Wilson (1975) profile or power-law profiles like those of Elson et al. (1987) fit the outermost parts of Milky Way and Magellanic Cloud GCs as well or better than classic King profiles. Furthermore, Webb et al. (2012b) compare King62 models fits to King66 (King 1966), Wilson75 (Wilson 1975), and Sérsic models (Sérsic 1968) for GCs in M87 and find that King66 models significantly underestimate cluster sizes, while Wilson75 fits are in close agreement with King62 measurements. However, we keep in mind that GCs outside the Local Group may have experienced different dynamical evolution histories given that their host galaxies may have undergone more violent merging and accretion histories (e.g., Baumgardt & Makino 2003) that may give rise to a larger variety of unusual GC surface brightness profiles. Our analysis will necessarily be less sensitive to the outer low-surface brightness outskirts of the NGC 1399 GCs than to their half light or core properties. Since all the aforementioned profiles are virtually identical in their inner parts (i.e., within their half-light radius; see McLaughlin & van der Marel 2005), we adopt the King62 profile for the rest of the analysis. The main reason is that for marginally resolved GCs the profile choices become rather unconstrained, and more complex models often diverge or give degenerate results (Barmby et al. 2007; McLaughlin et al. 2008; Harris et al. 2010), whereas the King62 profile provides the most robust measures of GC structural parameters for both marginally resolved and well-resolved targets.

4.2. The Fitting Routine

To derive the structural parameters of NGC 1399 GCs, we fit their surface brightness profiles using a modified version of the GALFIT package that includes the King profile as a fitting option (version 3.0, Peng et al. 2010, and references therein).

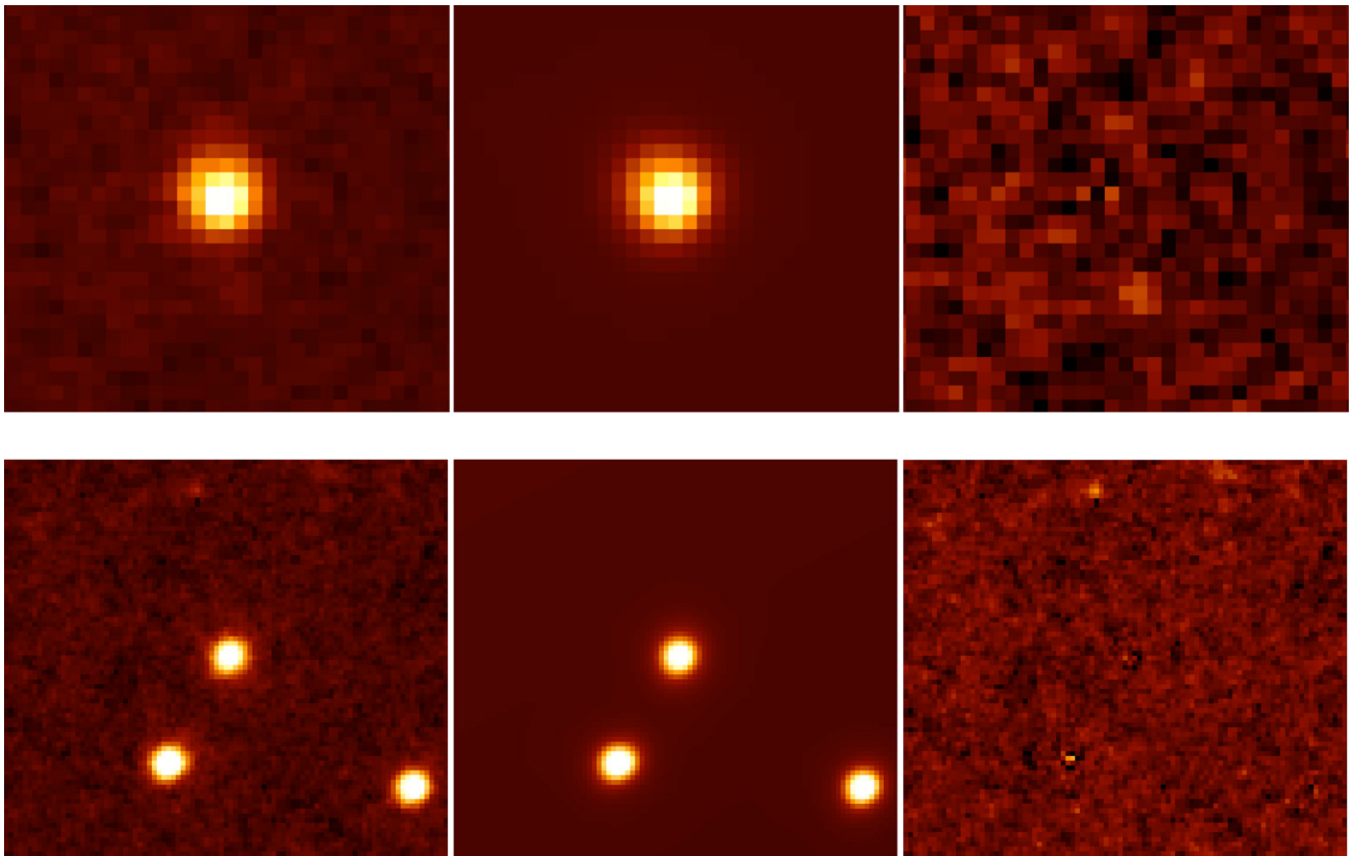

Figure 6. Postage stamp cutouts of typical examples of King profile fits from our fitting routine. The left panels show the data, and the middle panels illustrate the models, both shown with the same color stretch. The right panels are the residual maps with a 10 times larger color stretch to accentuate the residual noise, which is less than ∼1% for these particular cases. The field of view in the top panels is $\sim 1'' \times 1''$, while the imaged area in the bottom panels is $\sim 2\farcs5 \times 2\farcs5$.

(A color version of this figure is available in the online journal.)

Previous software packages such as ISHAPE (Larsen 1999), GRIDFIT (McLaughlin & van der Marel 2005), and KINGPHOT (Jordán et al. 2005) offer valid alternatives for measuring GC structural parameters. However, ISHAPE generally uses fixed King concentration parameters and deals with elliptical sources in a semianalytical way. These three routines do not allow for flexible fitting of multiple blended sources with various profile types plus a variable background component. Additional advantages of our code are the execution handling and speed, which allow us to efficiently conduct large numbers of artificial cluster experiments (see below).

We account for blended sources within the fit region of each GC and simultaneously fit profiles to sources that are less than five magnitudes fainter than the target within a radius of two FWHM and to sources less than three magnitudes fainter outside this region. At the same time, we match the contributions of the sky+galaxy surface brightness by fitting a surface within the same area. The code uses a χ^2 minimization scheme to simultaneously optimize the fit to each source and the local background surface brightness. Because some objects are blended with nearby very extended sources, we additionally use various profiles types for those blended objects, such as clearly extended nearby dwarf galaxies for which we choose the Sérsic profile (Sérsic 1968). Extended objects that have isophotal areas $\gtrsim$10 times larger than the fitting area are well approximated by a simple sloped background contribution. A representative example of the fit quality for a typical GC in NGC 1399 is shown in Figure 6.

4.3. Constructing the PSF Library

Equation (2) shows that detailed knowledge of the local PSF over the entire image is mandatory to obtain meaningful measurements of profile parameters, and the most realistic representation of the convolution product $P(\boldsymbol{r}) \otimes D(\boldsymbol{r})$ is provided in the form of a library of empirically measured PSFs (see discussion in Georgiev et al. 2009b). Such a library of effective PSF (ePSF) profiles based on repeated ACS observations of dense stellar fields was presented for several *HST*/ACS filters by Anderson (2005) and Anderson & King (2006). Because of the fully empirical approach to build such a library (Anderson & King 2000), this collection provides the best characterization of the ACS/WFC-PSF for our purposes, as it preserves the variations of high- and low-contrast features of the PSF with high spatial on-chip sampling. This is superior to the PSF modeling techniques provided by the TinyTim simulator[17] and other parametric PSF approximations (Jee et al. 2007), as well as building the PSF library from the science images themselves where the relative foreground stellar density is not sufficiently high to obtain a clean PSF star sample.

The ePSF library provides a set of 10×9 PSF profiles uniformly covering the WFC field of view. Each ePSF is oversampled by a factor of four to account for shifts of the source centroid with respect to the pixel center and applies only to the individual distorted ACS exposures ("flt" files). In order to transform the ePSFs into the final drizzled images, we need

[17] http://www.stsci.edu/software/tinytim/tinytim.html

to apply our data reduction process to the library itself. To this end we designed a custom software package (MultiKing;[18] see Paolillo et al. 2011) to overlay the Anderson PSF grid onto a set of empty WFC frames, reproducing the actual data frame properties (orientation, dither pattern, astrometry, etc.). The grid positioning was modified on each frame to preserve the sky coordinates of each PSF, properly accounting for geometric distortions that affect the WFC flt frames, as would be expected for a real source within a set of observations taken with our dithering pattern. Since each dither pattern is executed with slightly varying subintegration pointings, this procedure was applied to each individual pointing of the ACS mosaic. Finally, the dithered ePSF frames were combined together in the same way as the science frames, producing a drizzled effective PSF (drPSF) library for each individual ACS tile. The specific stellar PSF at a random location within our final images is chosen to be the nearest drPSF within the template grid. We use these drPSF libraries for the subsequent analysis. Our code was already implemented in the study of Goudfrooij (2012), who successfully used the drPSF approach to measure star cluster sizes in NGC 1316.

4.4. Artificial Cluster Experiments

Every attempt to determine the structural parameters of extragalactic GCs is affected by measurement uncertainties, parameter covariance, and other inherent systematic characteristics of the data set and measuring technique. To test the robustness of our measurements (under the assumption that the King62 profile describes the NGC 1399 GC profiles sufficiently well) and probe parameter correlations and systematics, we used our MultiKing code to create and add artificial star clusters to our ACS science frames and attempt to recover their structural parameters with our profile fitting routines using the exact same approach as for the analysis of NGC 1399 GCs. This process includes convolving the appropriate drPSFs of the corresponding ACS tile with King profiles of varying structural parameters and inserting the noise-corrected clusters at random locations in the eastern, southern, and central tiles of the ACS mosaic. In this way we include 1500 artificial clusters per tile in 15 runs each to avoid effects of artificial crowding. The input structural parameters cover a broad dynamic range that aims to sample crucial values around the resolution and confusion limits more densely. In particular, it covers the typical sizes of Galactic and LMC globular clusters.

The recovery quality of the core radius, r_c, half-light radius, r_h, and tidal radius, r_t, is illustrated in Figure 7. For each parameter we show the input versus output correlation, together with a "sliding-median" probability density estimate and the corresponding 1σ contours as well as the error-of-the-mean margin. The renormalized profile fit quality serves as a metric to divide our artificial cluster sample into low- and high-quality fits, the division of which is done at the renormalized reduced $\hat{\chi}^2 = 1$. This division generally corresponds to faint and bright sources. The corresponding histograms in the left panels of Figure 7 compare the input with the recovered parameter distribution and indicate biases in our measuring process. Our cluster experiments are consistent with the results presented in Carlson & Holtzman (2001). In particular, all our bona fide sample GCs have an integrated S/N $\gtrsim$ 100, in agreement with the minimum prescription of Carlson & Holtzman to measure sizes of marginally resolved GCs.[19] In the following, we discuss and quantify these systematics to provide numerical estimates of the reliability of the subsequent structural parameter analysis.

4.4.1. Recovery Fidelity of the King Core Radius

The top panels in Figure 7 show how our code recovers the King core radius, r_c. From the left panel, i.e., input versus output r_c diagram, it is evident that the spatial resolution of our data set becomes increasingly poorer at $r_c \lesssim 3$ pc, and we see nicely a "leveling off" of the relation toward smaller spatial scales. The reader should be aware that the logarithmic scaling in this plot is chosen to show exactly this physical limit and exaggerates this effect optically. In the right panel we plot the r_c difference relation, in the sense $\Delta r_c = r_{c,\rm out} - r_{c,\rm in}$, versus the recovered core radius $r_{c,\rm out}$. The graph illustrates that the measurements can be robustly corrected with a small systematic offset of the form $\langle \Delta r_c \rangle = 0.81 \pm 0.04$ pc with a mean standard deviation of $\bar{\sigma}_{1-30\,\rm pc} = 1.54$ pc, which is equivalent to the overall r_c measurement uncertainty in this range. While the Δr_c trend around the spatial resolution limit allows an almost linear correction, it is clear that the scatter in Δr_c increases toward larger r_c, which is due to the confusion limit of the data, e.g., blended sources, sky background fluctuations, etc. At this end we see a higher-order systematic trend that cannot be approximated with a simple offset. We therefore use the correction function

$$\phi_{r_c} = 0.731 - 5.563 \cdot 10^{-2} r_{c,\rm out} + 3.742 \cdot 10^{-3} r_{c,\rm out}^2 \qquad (4)$$

to fit the overall trend in Δr_c as a function of $r_{c,\rm out}$ and correct our r_c measurements for $r_{c,\rm out} \in [1, 30]$ pc. The function is shown as a dash-dotted curve in the top right panel of Figure 7 and approximates the probability density curve very well in the range $r_c \approx$ 2–20 pc, which we consider to be our high-confidence range for the King core radius measurements.

4.4.2. Recovery Fidelity of the King Tidal Radius

The tidal radius, r_t, probes the outskirts of the GC light distribution. Our tests recover r_t with good accuracy in the range between ~10 and 100 pc (see middle panels in Figure 7). The mean residual is $\langle \Delta r_t \rangle = 2.86 \pm 0.25$ pc, with an average standard deviation of $\bar{\sigma}_{10-100\,\rm pc} = 9.06$ pc. The lower limit is set by the starting value of our fitting routine, which is 10 times the initial core radius value, so that some clusters with a large core radius and a slightly larger tidal radius end up with an overestimated tidal radius because the numerical convergence of the code for fits with very similar core and tidal radii is internally defined by the core radius. Note that the tidal radius cannot be smaller than the core radius. For objects more extended than ~100 pc we run into background confusion and fit degeneracy problems, introduced by nearby diffuse galaxy components and satellite objects (which are fit as described in Section 4.2). Hence, the fits become poorly defined beyond such large tidal radii, simply because there is not a high enough signal-to-noise ratio in the low surface brightness wings of the

[18] The IDL source code to produce the drPSF library grid images is available at http://people.na.infn.it/~paolillo/Software.html.

[19] We also note that Carlson & Holtzman (2001) claim that S/N > 500 is required in order to fully recover all King model parameters for every type of GC out to a distance of ~40 Mpc, i.e., twice as far as NGC 1399. On the other hand, they state that S/N ≈ 100 is appropriate for, e.g., Virgo galaxies or less concentrated systems and that GC half-light radii are recovered with even better accuracy. Furthermore, our spatial sampling (pixel size) is ~3 times better than what was used in their study.

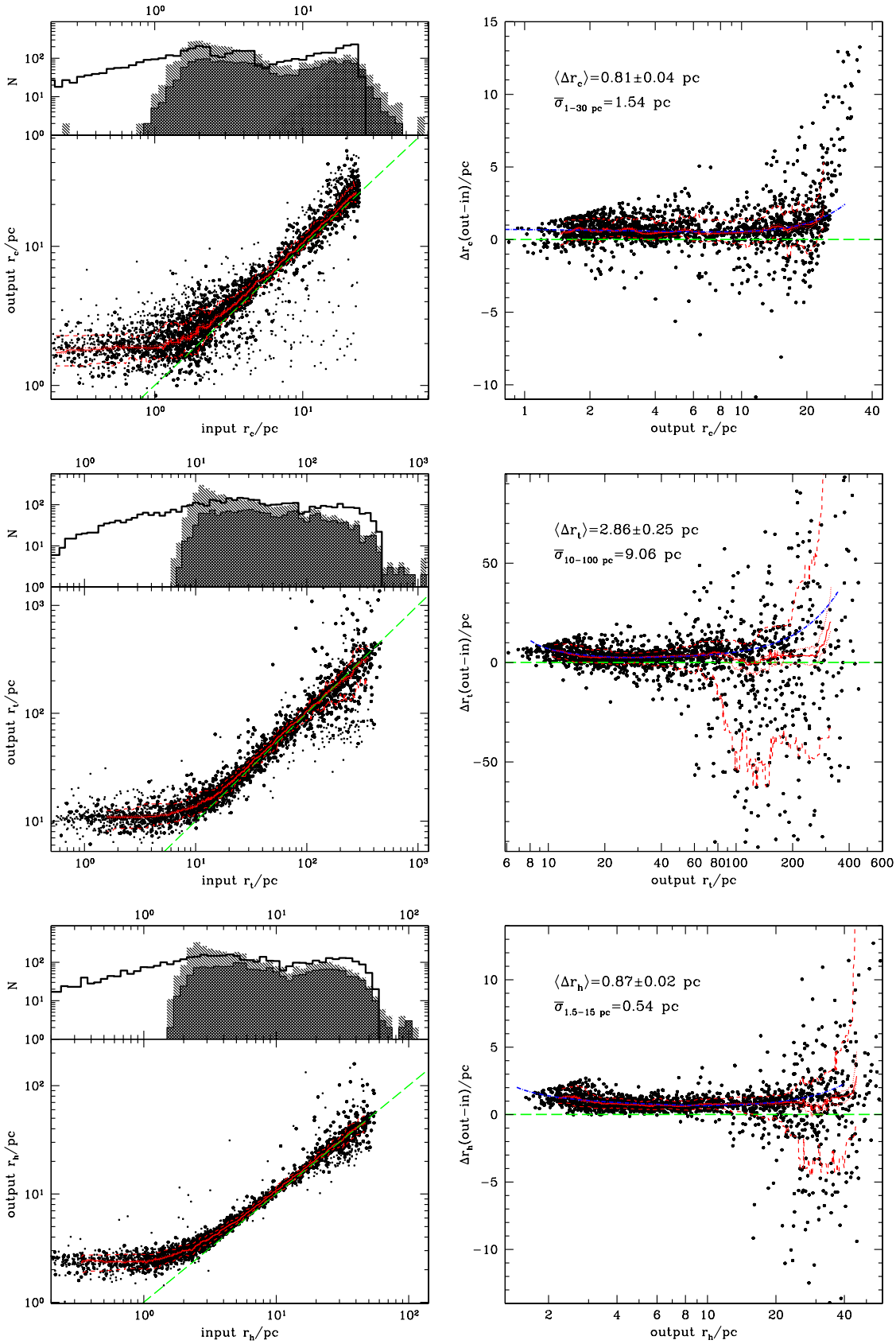

Figure 7. Recovery quality of King profile structural parameters (r_c, r_t, r_h) performed with an artificial star cluster. The left column shows the input vs. output parameter values and is divided into low-quality (small dots: $\hat{\chi}^2 > 1$) and high-quality (large dots: $\hat{\chi}^2 \leqslant 1$) profile fits. A dashed line indicates the equality relation, and a solid red curve is a sliding-median probability density estimate with its 1σ limits (dashed curves) and the error of the mean (dotted curves). The histogram subpanels show the input parameter distribution (open histogram) in comparison with the high-quality (double-shaded histogram) and low-quality (single-shaded histogram) profile fits. The right column shows the corresponding residual functions for each structural parameter as a function of the output value. Blue dash-dotted curves are correction functions that are fits to the data (see the text for details).

(A color version of this figure is available in the online journal.)

profiles. We approximate the corresponding residual trend with the following two-component correction function:

$$\phi_{r_t} = \begin{cases} 0.646 + 22.458\,(r_t - 5.581)^{-0.86} & \text{if } r_t \in [10, 25), \\ 2.078 + 6.675 \cdot 10^{-3}\,(r_t - 1.11) + \\ +2.591 \cdot 10^{-4}\,(r_t - 1.11)^2 & \text{if } r_t \in [25, 100], \end{cases} \quad (5)$$

which is valid in $r_t \in [10, 100]$ and robustly follows the probability density estimate out to the extreme edges of the parameter range.

4.4.3. Recovery Fidelity of the Half-light Radius

The GC half-light (or effective) radius, r_h, is a structural parameter that emerges from the correlation of the King core and tidal radius, as described by Equation (3), and encircles 50% of the total GC light. The half-light radius is relatively stable throughout the GC dynamical evolution and is predicted to evolve much slower with time ($r_h \propto t^{2/3}$) than the tidal and core radius (Hénon 1973, 1975; Elson et al. 1987; Murphy et al. 1990; Murray & Lin 1992). One major advantage of r_h is its relatively effortless accessibility in more distant stellar systems, and because of its slow evolution it provides the most reliable measure of the true size distribution function of the extragalactic GC system. Formally, the GC half-light radius, r_h, is defined as

$$2\pi \int_0^{r_h} \mu(\boldsymbol{r})\boldsymbol{r}d\boldsymbol{r} = \pi \int_0^{\infty} \mu(\boldsymbol{r})\boldsymbol{r}d\boldsymbol{r}, \quad (6)$$

and can be evaluated with the integral form of the King profile, which can be written as

$$2\pi \int_{r_1}^{r_2} \mu_{\rm K}(\boldsymbol{r})\boldsymbol{r}d\boldsymbol{r} = \left[\frac{kr_c}{\varrho} \left\{ \varrho \arctan\left(\frac{\boldsymbol{r}}{r_c}\right) + r_c \left(\boldsymbol{r} - 2\sqrt{\varrho}\, \ln\left(2\boldsymbol{r}\sqrt{\varrho} + 2r_c^2 \sqrt{1 + \frac{r_t^2}{r_c^2}} \sqrt{1 + \frac{\boldsymbol{r}^2}{r_c^2}} \right) \right) \right\} \right]_{r_1}^{r_2} \quad (7)$$

where $\varrho = r_c^2 + r_t^2$. Since the half-light radius r_h cannot be written in a closed analytic form from Equations (6) and (7), it has to be evaluated numerically. Hence, we determine r_h from the direct numeric integration of the King profile for each individual cluster and thus probe immediately the influence of parameter correlations between r_c and r_t on the integrated luminosity. The bottom panels of Figure 7 show that the average bias of the half-light radius is $\langle \Delta r_h \rangle = 0.87 \pm 0.02$ pc, with an average standard deviation of $\bar{\sigma}_{1.5-15\,\rm pc} = 0.54$ pc. This is in excellent agreement with the results of Harris (2009), who found $\sigma_{r_h} = 1.1$ pc as the mean uncertainty for size measurements of GCs at a distance of ~40 Mpc based on similar data of distant brightest cluster galaxies (BCGs), which are roughly twice as far away as NGC 1399. The reduced mean uncertainty of r_h is likely due to parameter correlations between r_c and r_t, the uncertainties of which compensate each other and leave r_h a very reliable parameter of GC size. The results of our artificial cluster experiments indicate that we can measure and correct r_h reliably for $r_h \in [1.5, 19]$ pc. We compute the corresponding correction function of the form

$$\phi_{r_h} = \begin{cases} 0.33 + (r_h - 0.354)^{-4.26} & \text{if } r_h \in [1.5, 7), \\ 0.449 - 5.766 \cdot 10^{-2}\,(r_h - 0.1) \\ +5.869 \cdot 10^{-3}\,(r_h - 0.1)^2 & \text{if } r_h \in [7, 19]. \end{cases} \quad (8)$$

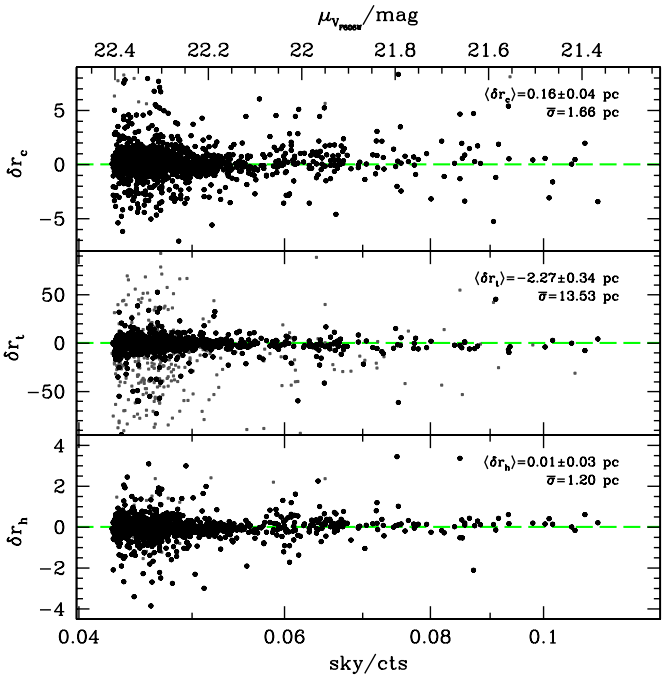

Figure 8. Illustration of the residuals around the correction functions (see Equations (4), (5), and (8)) as a function of background surface brightness. High- and low-quality fits are depicted as gray and black dots, respectively, and are defined as fits with a reduced χ^2 below and above unity. Mean residuals and dispersion are given in each panel. Caon et al. (1994) measure the *B*-band surface brightness profile of NGC 1399 out to an ~15′ galactocentric radius. We use the numbers from Sandage (1975), who reports $B - V \simeq 0.95$ to 0.98 mag in the range 54.″3–107.″8 from the center of NGC 1399 to obtain a rough estimate of the *V*-band surface brightness.

(A color version of this figure is available in the online journal.)

In summary, we now understand the fidelity and limitations of our structural parameter measurements and move on to test the influence of the variable background surface brightness in our ACS mosaic.

4.4.4. Influence of the Variable Galaxy Background

After correcting for biases in our measuring procedure, we explore in the following the influence of the variable galaxy surface brightness in the studied field on our structural parameter measurements. To do so, we compute the residuals with respect to the correcting functions ϕ_{r_i} in Figure 7 in the form $\delta r_i = (r_{i,\rm out} - r_{i,\rm in}) - \phi_{r_i}$, where the index i stands for the core, tidal, and half-light radii, respectively. The residuals are then plotted in Figure 8 as a function of the background counts. All our measurements are shown in Figure 8; however, only the values within the confidence limits of Equations (4), (5), and (8) are considered in the computation of the mean residual statistics. This exercise shows that our GC profile fitting routine accounts very robustly and without any significant residual systematic for the variable background. Our tests probe surface brightness levels fainter than $\mu_{V_{\rm F606W}} \gtrsim 21.4$ mag, which corresponds to galactocentric radii $r \gtrsim 30''$, and we expect that the final measurements are reliable without further corrections to within the quoted uncertainties of our artificial cluster experiments within the above $\mu_{V_{\rm F606W}}$ range.

4.5. Comparison with ACSFCS Measurements

In the following we compare our measurements to the most recent GC half-light radius measurements in NGC 1399 based

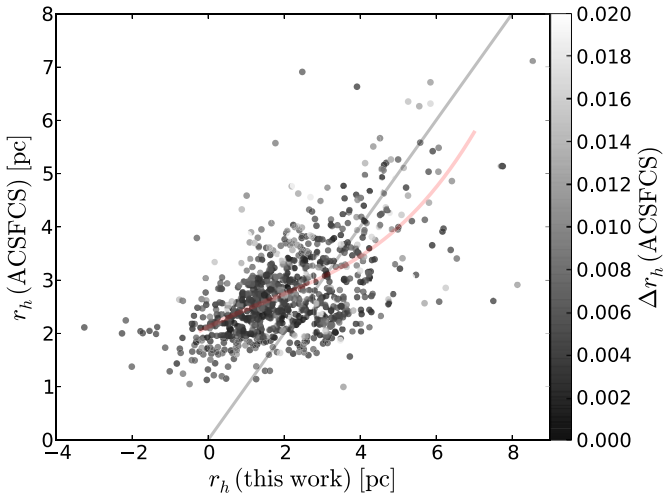

Figure 9. Comparison of GC half-light radius measurements from this work and the ACSFCS (see Jordán et al. 2007; Masters et al. 2010) for the same target GCs in NGC 1399. The gray line shows the one-to-one relation. The gray scale parameterizes the ACSFCS measurement uncertainties, Δr_h, which are computed as the square root of the square sum of the individual uncertainties in the F475W and F850LP filters. The red line is a third-order polynomial approximation to the data.

(A color version of this figure is available in the online journal.)

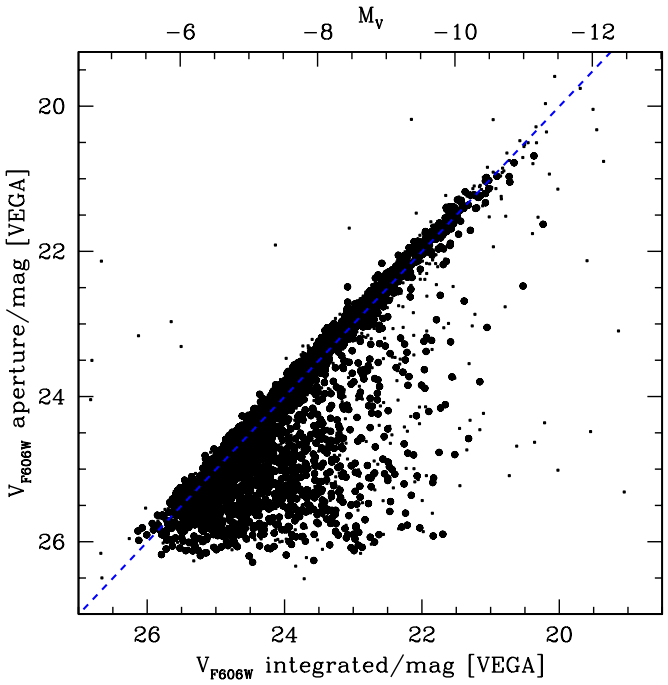

Figure 10. Comparison of total object luminosities determined via aperture photometry and direct integration of their surface brightness profile. Both magnitudes are in the Vega system and are corrected for Galactic foreground reddening with $A_{F606W} = 0.038$ mag. The top ordinate indicates the absolute M_V at the distance of Fornax. The blue dashed line shows the equality relation.

(A color version of this figure is available in the online journal.)

on the ACSFCS (see Jordán et al. 2007), which observed the galaxy with one central pointing. The ACSFCS GC half-light radius measurements were conducted with the KINGPHOT software (Jordán et al. 2005) and are restricted to the brightest GCs with $z \leqslant 23.35$ mag and colors $0.6 \leqslant (g - z) \leqslant 1.7$ mag. The ACSFCS data are composed of $2 \times 565 + 90$ s exposures in F850LP and 2×380 s exposures in F475W. Compared to our 4×527 s optimally dithered F606W observations, the ACSFCS data therefore have a somewhat lower S/N at an equivalent GC luminosity (because of lower system throughput in F475W and F850LP) and have a more sparsely sampled PSF because of their two-step dither pattern (Jordán et al. 2005, 2007). We take the ACSFCS GC half-light radii published as part of the study presented in Masters et al. (2010) and use the arithmetic mean of their GC half-light radius measurements in the F475W and F850LP filters and select only GC candidates that were assigned a GC probability of $p_{GC} \geqslant 0.5$ (see also Jordán et al. 2009).

Figure 9 shows the direct comparison between the two samples where we find no significant offset beyond $r_h \approx 2$ pc. However, at smaller half-light radii, the influence of the correction function from Equation (8) (see also Figure 7) becomes increasingly apparent as the ACSFCS data tend to be biased toward larger values relative to our measurements. This is primarily because the ACSFCS measurements are not corrected for measurement systematics by means of artificial cluster experiments as in our procedure (see Section 4.4.3). We parameterize the gray shading of data points in Figure 9 with the measurement uncertainties, σ_{r_h}, of the ACSFCS data. The main trend of the comparison is approximated by a third-order polynomial and depicts the shape of the correction function. The rms around this relation is 0.77 pc, and with our measurement uncertainty of 0.54 pc from the artificial cluster experiments described in Section 4.4.2, we obtain $\Delta_{\rm total} = \sqrt{\sigma_{r_h}(\mathrm{ACS})^2 - \sigma_{r_h}(\mathrm{this\ work})^2} \approx 0.55$ pc, which we regard as the total statistical uncertainty when comparing individual GC half-light radius measurements from various studies using different techniques.

5. RESULTS

We use our surface brightness profile (SBP) fitting routine described in Section 4.2 to measure the structural parameters of all sources from our photometric input catalog (see Section 3) and calibrate them with the correction functions ϕ_{r_i} derived in Section 4.4 (see Equations (4), (5), and (8)). Because of the higher measurement fidelity of the half-light radius, we use r_h in the subsequent analysis and refer to it as GC size, unless stated otherwise. We point out that to address other specific scientific topics, such as measuring the binary star formation efficiency via LMXB population analysis, other parameters such as the core radius and central surface brightness proved to be more diagnostic than r_h (Paolillo et al. 2011).

5.1. Total Object Magnitudes

To investigate correlations of structural parameters with GC brightness it is important to compute accurate total luminosities for our object sample. In Section 3.2 we corrected our aperture photometry with a generic aperture correction term to compensate for the light outside the $r = 0\farcs24$ photometry radius, which delivered the highest photometric S/N and served as a first guess for the structural parameter fitting routines. With our structural parameter measurements in hand we can now directly integrate the surface brightness profile of all targets and determine their total luminosities and compare them with the traditionally determined aperture magnitudes. Figure 10 shows the direct comparison of total Vega magnitudes measured via corrected aperture photometry and integrated SBP luminosities. Small and large dots are defined as in Figure 7 for low- and high-quality fits of the surface brightness profile. Figure 10 shows that the vast majority of our sample aligns very well with the one-to-one relation, which is because most of our sample objects are marginally resolved GCs. Clearly resolved objects

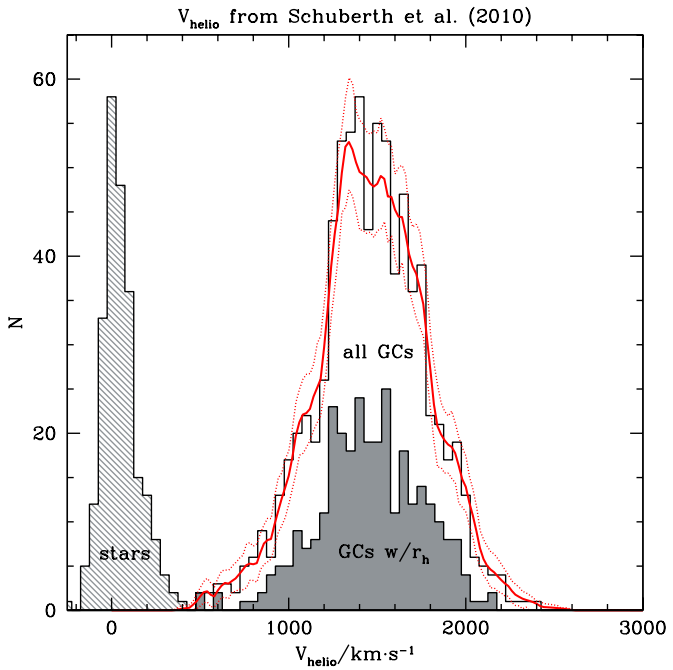

Figure 11. Radial velocity distribution of objects toward the core regions of the Fornax cluster for which Schuberth et al. (2010) provide $v_{\rm helio}$ measurements. The open histogram are all GCs with such measurements, and the shaded histogram shows the $v_{\rm helio}$ distribution of matched GCs for which we measured structural parameters. The hatched histogram shows the $v_{\rm helio}$ distribution of foreground stars from Schuberth et al. (2010). The solid and dotted red curves show the probability density estimates to the entire GC sample together with their 90% confidence limits.

(A color version of this figure is available in the online journal.)

scatter to the right of the one-to-one relation and have brighter integrated magnitudes and have too faint aperture photometry counterparts. Their total aperture magnitudes at the GCLF turnover M_V(GCLF) $\simeq -7.5$ mag are up to $\sim$0.5–2 mag fainter than the corresponding integrated SBP luminosities. In general, this is due to an average correction that is applied to all GCs when measuring GC luminosities via aperture photometry. This is direct evidence that for partially resolved and clearly resolved objects an average aperture correction term is not sufficient to determine their total luminosities. Note also that there are virtually no outliers left for the one-to-one relation, which is visual assurance of our SBP fitting quality.

The study of Kundu (2008) has previously claimed that certain GC parameter correlations, such as the color–luminosity relation for bright blue globular clusters, may be the result of inappropriately applying average aperture corrections to multipassband photometry object samples with widely varying structural parameters. Although our structural analysis is based on only the F606W filter, to avoid such problems in what follows, we use the directly integrated SBP magnitudes for the subsequent analysis and point to the works of Peng et al. (2009) and Harris (2009) for a more detailed discussion of this filter-dependent aperture correction issue.

5.2. Radial Velocity Information

In the following we use radial velocity measurements from Schuberth et al. (2010) to define a clean GC subsample which is consistent with the systemic velocity and GCS velocity dispersion in the center of Fornax. Figure 11 shows the distribution of heliocentric radial velocities, $v_{\rm helio}$, for foreground stars and bona fide GCs, as well as the subsample of GCs for which we measured structural parameters. We match 306 out of the 790 GCs for which Schuberth et al. (2010) provide $v_{\rm helio}$ values that have structural parameter measurements from our analysis. Most of the remaining objects are at larger galactocentric radii, and a small fraction has bad profile fits due to detector edge effects and confusion with very bright nearby sources. The distribution of the matched GCs, illustrated in Figure 11, shows that they representatively sample the total radial velocity distribution of the Schuberth et al. sample. We also match nine stars out of the 236 confirmed by Schuberth et al. (see the hatched histogram around $v_{\rm helio} \approx 0$ km s^{-1} in Figure 11) and study the distribution of structural parameters of false positives introduced by the foreground stellar population.

5.3. GC Half-light Radius as a Function of Luminosity

Before analyzing GC size variations as a function of GC color and galactocentric radius we need to make sure that potential observational biases are not influencing our result. One such bias is a correlation between GC size and luminosity; such a correlation can introduce systematics in the size distribution function for photometrically selected samples because of changing M/L ratios for stellar populations with different ages and/or metallicities. The population synthesis models of Bruzual & Charlot (2003) and Maraston (2005) give roughly a factor of two difference between the stellar $(M/L)_V$ ratios for 13 Gyr old stellar populations with metallicities [Z/H] $= -1.5$ and -0.5 dex, which roughly correspond to the mean metallicities of the GC subpopulations in the Milky Way and other massive spiral and elliptical galaxies (e.g., Peng et al. 2006). For a magnitude-limited sample such a M/L difference would correspond to an $\sim$0.75 mag offset in completeness for a uniformly old GC population.

We plot the GC size, i.e., half-light radius, r_h, versus luminosity in Figure 12. Running-median curves with their 90th percentile limits show that there is no indication for any significant GC size–luminosity relation for the entire GC sample. At a constant M/L ratio this corresponds to $L \propto r_h^3 \rho$ and implies, therefore, that the stellar density is directly proportional to the GC size, i.e., $\rho \propto r_h^{-3}$. Linear and quadratic least squares fits (dashed blue lines in Figure 12) do not show any significant slopes for the entire sample, and neither linear nor higher-order fits are statistically preferred over the other.

Splitting the entire GC sample at a projected galactocentric radius of $R_{\rm gal} = 20$ kpc into "inner" and "outer" subpopulations, we spot a few interesting trends. First, at intermediate luminosities ($22 \lesssim V_{\rm F606W,0} \lesssim 24.0$ mag) the inner sample contains fewer extended GCs with half-light radii $r_h \gtrsim 4$ pc than the outer sample. The cause is determined not to be due to the varying galaxy background and/or completeness (see Section 4.4.4) or due to lower statistics in the galaxy center (as there are actually more GCs) and might be due to the preferred disruption of extended GCs in the inner regions of NGC 1399. The fact that we see virtually no extended GCs more massive than the GCLF turnover at $V_{\rm F606W,0} \approx 24.0$ mag indicates that disruption or tidal limitation (see Section 6.1) may occur more frequently for low-mass GCs and that high-mass GCs are more prone to dynamical friction and orbital decay (e.g., Lotz et al. 2001). Second, we observe a weak indication for a size–luminosity relation for GC brighter than $V_{\rm F606W,0} \approx 22.0$ mag, predominantly for the inner subsample. We fit this subsample separately with a linear relation that yields a significant slope of $r_h \propto (-0.6 \pm 0.2)\, V_{\rm F606W,0}$, which is reminiscent of the transition from the GC regime without any size–luminosity relation below $M_\star \approx 10^6\ M_\odot$ to the

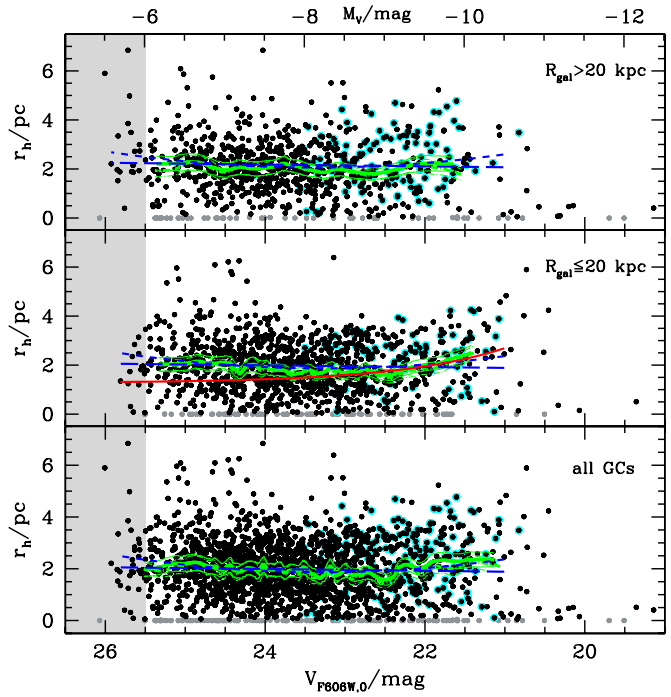

Figure 12. GC half-light radius as a function integrated $V_{\rm F606W,0}$ luminosity for outer clusters (top panel), inner clusters (middle panel), and the entire GC sample (bottom panel). Black dots are resolved GC, while gray dots mark unresolved objects. Solid green curves show the sliding-median trends of resolved data together with their 90% percentile limits. Dashed curves are the corresponding trends for all objects. Linear and quadratic least squares fits to the resolved cluster data are shown as long-dashed and short-dashed lines, respectively. The shaded region at faint luminosities ($V_{\rm F606W,0} > 25.5$ mag) indicates the region where the photometric preselection becomes significantly incomplete. Cyan data mark bona fide GCs confirmed by their radial velocity.

(A color version of this figure is available in the online journal.)

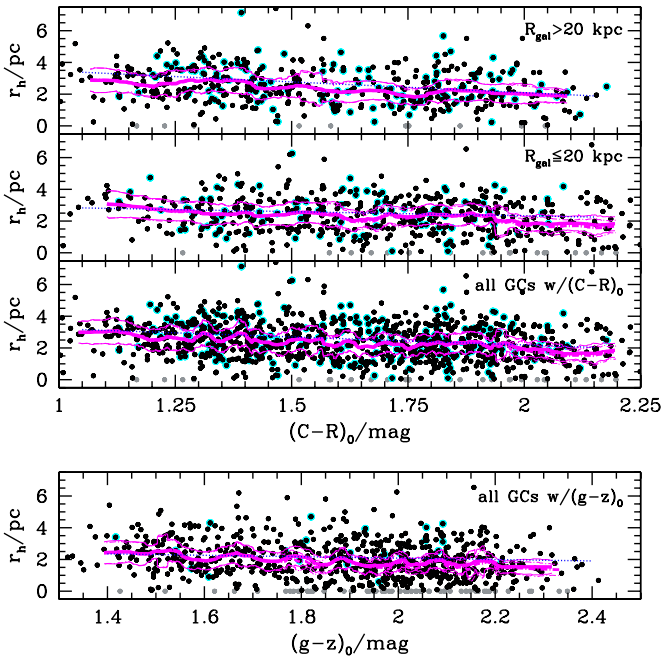

Figure 13. Globular cluster half-light radius, r_h, as a function of photometric color. Top panel: The bottom subpanel shows the distribution of half-light radii for all GCs with ground-based $(C-R)_0$ color information from Schuberth et al. (2010). The two upper subpanels show the size distribution divided in projected galactocentric distance at $R_{\rm gal} = 20$ kpc for the inner and outer samples. Bottom panel: GC half-light radii as a function of the $(g-z)_0$ color based on *HST* photometry taken from Kundu (2008). Solid thick and thin curves illustrate the running median and the 1σ limits, respectively, of the r_h distribution in each subpanel. We show the unresolved clusters as gray dots, which are not considered in computing the solid curves. Including those unresolved sources results in corresponding relations shown as dash-dotted curves. Cyan data illustrate bona fide GCs confirmed by their radial velocity.

(A color version of this figure is available in the online journal.)

size–stellar mass relation ($r_h \propto M_\star^{0.8}$) of more massive compact stellar systems such as ultra-compact dwarfs (UCDs; e.g., Taylor et al. 2010; Misgeld et al. 2011; Misgeld & Hilker 2011). This relation is indicated in the middle panel as a thin red curve and is a good representation of the general trend of the data. We point out that the subsample of confirmed GCs with $v_{\rm helio}$ measurements (cyan dots in Figure 12) is consistent with this trend.

Despite the fact that we detect a weak size–luminosity relation for massive GCs we stress that the majority of our sample, in particular the intermediate-luminosity to faint-end part, does not show any such relation. We are therefore safe to apply a simple magnitude cut to our data without introducing systematics in the GC size–color relation, which we discuss in the following.

5.4. GC Half-Light Radius as a Function of Color

We add photometric color information to our GC size measurements and search the $C-R$ color database presented in Schuberth et al. (2010) to find 1811 sources that match our final catalog within a $1''$ matching radius. The Schuberth et al. photometric catalog is a combination of (1) the Dirsch et al. (2003) Washington photometry, obtained for one central pointing with a field of view of $36' \times 36'$ using the MOSAIC camera on the CTIO-Blanco 4 m telescope, and (2) the photometry from Bassino et al. (2006), which covers additional fields in the outskirts around NGC 1399, also imaged with the MOSAIC camera. In addition, we combine our GC size measurements with the *HST* photometry of Kundu (2008) and find 1258 matches within a $1''$ search radius, all of which are within the field of view of only one central *HST* pointing. These two data sets have very different completeness limits and spatial resolution characteristics, so we use them only to search for differential trends in each data set separately.

We note that on the basis of the ACSVCS data, Jordán et al. (2005) have demonstrated that the mean trend of increasing half-light radius toward bluer GC colors does not strongly depend on the host galaxy $(g-z)_{\rm gal}$ color, except for the very bluest galaxies with $(g-z)_{\rm gal} < 1.52$ mag, where the GC size difference appears to vanish (see a more detailed discussion in Section 6). In that sense, the GC system of NGC 1399 should be representative for most massive galaxies.

In Figure 13 we show the trends of GC size, i.e., half-light radius, r_h, versus $C-R$ color from the MOSAIC study and the $g-z$ color from the *HST* central pointing and find significant trends in both colors of increasing GC sizes toward bluer GC colors. This is a different depiction of the well-known size difference between blue and red GCs discussed in previous studies (e.g., Kundu & Whitmore 1998). For both photometry samples of resolved clusters we find $r_h \propto (-0.44 \pm 0.15) \times (g-z)$ for the *HST* data and $r_h \propto (-0.78 \pm 0.15) \times (C-R)$ for the wide-field MOSAIC sample. For the entire MOSAIC sample the average r_h gradient corresponds to a mean size difference of $\sim$15% between the peak colors $C-R = 1.3$ and 1.8 mag. Since the MOSAIC data cover a wide field of view, we determine the GC size variation as a function of color for two subsamples split at 20 kpc in projected galactocentric distance into inner and

Table 2
Photometric Selection of Blue and Red GCs

	Blue GCs	Red GCs	Ref.
Ground-based	$T1 < 23$	$T1 < 23$	1
data	$1.0 \leqslant C - R < 1.65$	$1.65 \leqslant C - R < 2.2$	
HST data	$z < 22.5$	$z < 22.5$	2
	$1.3 \leqslant g - z < 1.9$	$1.9 \leqslant g - z < 2.5$	

References. (1) Bassino et al. 2006; (2) Kundu 2008.

outer samples. We find that the r_h gradient is stronger for the outer sample (i.e., $r_h \propto (-0.89 \pm 0.22) \times (C - R)$) compared to the inner variation (i.e., $r_h \propto (-0.65 \pm 0.22) \times (C - R)$), which corresponds to a physical size variation of ∼12% and ∼17%, respectively. If we use only radial-velocity-confirmed GCs, we obtain a much more significant r_h change, namely, $r_h \propto (-0.52 \pm 0.50) \times (C - R)$ for the inner MOSAIC sample and $r_h \propto (-1.36 \pm 0.45) \times (C - R)$ for the outer MOSAIC sample. This corresponds to a physical difference of ∼10% and ∼23%, respectively. The overlap between the radial velocity information and the *HST* photometry sample from Kundu is too small to derive any robust r_h gradient values. However, for illustration purposes we mark all bona fide GCs confirmed by their $v_{\rm helio}$ as cyan dots in Figure 13 and find no significant differences in their GC size–color distributions down to the limiting magnitude of $V \approx 23.5$ mag, which marks the typical limit of spectroscopic studies.

5.5. GC Half-Light Radius as a Function of Projected Galactocentric Radius

Due to the wide field coverage of our ACS mosaic we are now in the position of determining the change of the classic size difference between blue and red GCs as a function of projected galactocentric radius, $R_{\rm gal}$, in much greater detail. To begin with, we use the photometric parameters summarized in Table 2 to define the blue and red GC subsamples. The top panel of Figure 14 shows the corresponding GC size versus $R_{\rm gal}$ distribution for all GC candidates. Taking the entire GC sample for which structural parameters were measured and calibrated (see Section 4), we observe several interesting regimes with constant and gradually changing GC sizes. First, GCs in the inner ∼10 kpc become, on average, larger as a function of $R_{\rm gal}$, while GCs at larger galactocentric distances ($\gtrsim$10 kpc) show no significant GC size–$R_{\rm gal}$ relation. This is illustrated by the black curves, which depict the sliding median together with error-of-the-mean margins. Second, plotting the median size trends for the blue and red GC subpopulations separately (middle panel of Figure 14) reveals the well-known GC size difference of ∼20% in the central parts of NGC 1399, i.e., $R_{\rm gal} \lesssim 10$ kpc (e.g., Kundu & Whitmore 1998; Jordán et al. 2005). Except for the range $R_{\rm gal} \approx$ 14–20 kpc, this size difference prevails at large galactocentric distances out to ∼30–40 kpc. The bottom panel shows the ratio of the median GC sizes for blue and red clusters in the sense $\mathrm{med}(r_{\rm h,red})/\mathrm{med}(r_{\rm h,blue})$. This mean ratio for the whole $R_{\rm gal}$ range is 0.82 ± 0.11. The existence of a GC size difference at large $R_{\rm gal}$ is direct evidence that this difference cannot be solely due to a projection effect as suggested by Larsen & Brodie (2003). Instead, it has to have its origin in at least one other internal or external parameter that determines the GC size and/or its evolution. The simulations of Sippel et al. (2012) suggest that this size difference is mainly due to GC internal evolution related to the impact of metallicity effects on

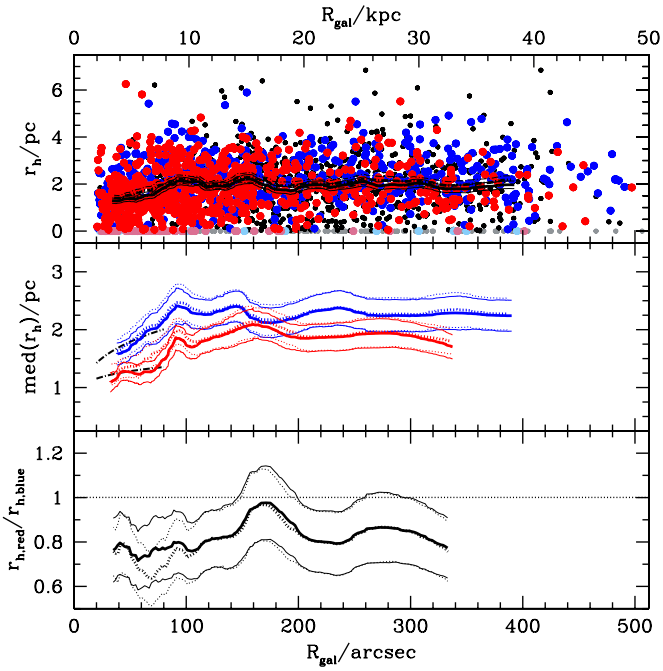

Figure 14. Globular cluster half-light radius, r_h, as a function of projected galactocentric distance, $R_{\rm gal}$. Top panel: All measurements for individual GCs. Blue and red dots are GCs that were classified as members of the blue and red GC subpopulations by their $(C - R)$ or $(g - z)$ colors (see Table 2). Black dots show GCs with structural parameter measurements that either have no ground-based colors or fall outside the fields of the corresponding studies that provide such colors (see text for details). The solid curves show the running median with 1σ error of the mean margins for the entire GC sample. The dot-dashed curves are the corresponding relations excluding unresolved objects, i.e., $r_h > 0$ pc. Middle panel: Running-median relations for blue and red GC subpopulations illustrated as blue and red curves, respectively. The dotted relations exclude unresolved objects. Thin curves show the 1σ error of the mean. Black dash-dotted curves indicate the GC size–$R_{\rm gal}$ relations for blue and red GCs in M87 as derived by Madrid et al. (2009). Bottom panel: The ratio of the median half-light radii between red and blue GCs as a function of projected galactocentric distance with the corresponding 1σ uncertainties and the same relations excluding unresolved objects as dotted curves. Note that the bottom abscissa and those in between the panels show the galactocentric radius in arcseconds, while the top abscissa indicates the physical scale in kiloparsecs assuming a Fornax distance of 20.13 Mpc.

(A color version of this figure is available in the online journal.)

stellar evolution combined with the GC dynamical evolution under the influence of mass segregation.

In the middle panel of Figure 14 we show the comparison with the GC size–$R_{\rm gal}$ relations for blue and red GCs in M87 as derived by Madrid et al. (2009). Similar conclusions have been reached by Paolillo et al. (2011), Blom et al. (2012), and Webb et al. (2012a). Within the $R_{\rm gal}$ coverage of the single central ACS pointing that these authors have used for their analysis, the agreement between their M87 and our NGC 1399 GC size trends is remarkably good.

6. DISCUSSION

6.1. Inner versus Outer GC System of NGC 1399

The significant GC size–luminosity relation of the inner 10 kpc that disappears in the outer regions may indicate a transition in the predominance of various mechanisms at different galactocentric radii that shape the GC sizes and thus their evolution as a system. Since the transition does not depend on GC color, i.e., blue and red GCs show that same r_h–$R_{\rm gal}$ relation, external dynamical effects are the most

probable explanation (e.g., dynamical friction of massive GCs that quickly sink into the core regions of the inner galaxy, tidal harassment of low-mass GCs by dwarf halos in the outer halo regions, etc.). While detailed numerical modeling of these effects goes beyond this work, we point out that our data set is ideal to conduct detailed analyses such as those presented in Vesperini & Zepf (2003) and Webb et al. (2012b, 2013). We note that the mean r_h for all resolved sources within $20'' < R_{\rm gal} < 120''$ is 1.95 ± 0.06 pc, i.e., significantly smaller than the mean value for the entire GC system of $\langle r_h \rangle = 3.21 \pm 0.07$ pc.

To test whether the stellar mass distribution in NGC 1399 is sufficient to produce the GC r_h–$R_{\rm gal}$ trend (see Figure 14), we use the surface brightness profile data obtained as part of the Carnegie–Irvine Galaxy Survey (CGS; see Ho et al. 2011; Li et al. 2011) to compute the local instantaneous Jacobi radius of GC, r_J, as a function of galactocentric radius out to $\sim 280''$ (i.e., $\sim$28 kpc), which corresponds to the maximum sampling radius of CGS. The Jacobi radius marks the point at which the gravitation forces exerted on GC member stars due to the GC potential and that of its host galaxy are equal but opposite in direction. The Jacobi radius can be expressed as

$$r_J = R_{\rm gal} \left(\frac{m_{\rm GC}}{2\mathcal{M}_{\rm gal}} \right)^{1/3} \quad (9)$$

and is a robust representation of the instantaneous GC tidal radius that is induced by the surrounding tidal field (Innanen et al. 1983; Bertin & Varri 2008; Renaud et al. 2011; Webb et al. 2013).

We proceed with computing the NGC 1399 mass distribution profile using the CGS data[20] and the recipes outlined in Bell et al. (2003) to convert photometric colors into stellar mass-to-light ratios as a function of galactocentric radius (see also Zibetti et al. 2009; Into & Portinari 2013). We compute the $\mathcal{M}_\star/L_V$ profile through linear interpolation of predictions for a 13 Gyr old stellar population with variable metallicity, which is set by the measured photometric color profile of NGC 1399, using the 2007 update of the Bruzual & Charlot (2003) simple stellar population (SSP) models. With the radial trend for $\mathcal{M}_\star/L_V$ we then derive the corresponding relation for the stellar mass

$$\log(\mathcal{M}_\star) = \log(\mathcal{M}_\star/L_V)_r - 0.4[m_V(r) - D_L - M_{V,\odot}] \quad (10)$$

enclosed in $R_{\rm gal} = r$, where $m_V(r)$ is the integrated magnitude derived from the galaxy surface brightness profile, D_L is the luminosity distance, and $M_{V,\odot} = 4.83$ mag is the absolute v-band magnitude of the Sun. With Equation (9) and the derived stellar mass profile of NGC 1399 from Equation (10), we determine the instantaneous Jacobi radii for GCs with a total mass of $m_{\rm GC} = 10^3$, 10^4, and 10^5 $M_\odot$ using the results from Baumgardt et al. (2010) and Ernst & Just (2013), who determine the typical ratios between half-light and Jacobi radii with minimum, mean, and maximum values of $\log(r_h/r_J) = -1.5$, -1.0, and -0.5 for Milky Way GCs. The extremes of the r_h/r_J distribution are representative of GCs that are under- and overfilling their Roche lobes, respectively.

We also compute the GC stellar masses using the differential $\mathcal{M}_\star/L$ predictions from the GALEV SSP models (Kotulla et al. 2009), assuming uniformly old GC ages ($t_{\rm GC} = 13$ Gyr) and using the $g-z$ and $C-T1$ GC colors to account for $\mathcal{M}_\star/L$ variations as a function metallicity. For GCs that lack color information we adopt the median $\mathcal{M}_\star/L$ of the GC sample for which photometric colors are available.

We overplot the corresponding expectation trends for r_h as a function of galactocentric radius in Figure 15 and use the color shading to parameterize GC mass. Consistent with Figure 12, we see no preferred GC mass scale at a given galactocentric radius. We observe that none of the curves reproduces the break at 10 kpc of the r_h–$R_{\rm gal}$ profile and its flatness at large galactocentric radii. The stellar mass density distribution is clearly not sufficient and requires an additional mechanism to limit GC sizes at large $R_{\rm gal}$. This could, in principle, be achieved by an exotic eccentricity distribution function of GC orbits, which would bring the outer clusters into the inner galaxy on preferentially radial orbits (see Webb et al. 2013). An alternative explanation for the observed situation could be an additional tidal limitation of GCs in the outskirts of the galaxy, which could be realized in two different ways.

1. The first is by an additional mass component in the form of a dark matter density profile of the Navarro–Frenk–White (NFW) type $\rho(r) = \rho_0/[(r/R_s)(1+r/R_s)^2]$ (Navarro et al. 1996), where the total mass inside radius $R_{\rm gal}$ is given by

$$\mathcal{M}_{\rm DM}(< R_{\rm gal}) = 4\pi \int_0^{R_{\rm gal}} r^2 \rho(r) dr \quad (11)$$
$$= 4\pi\rho_0 R_s^3 \left[\ln\left(\frac{R_s + R_{\rm gal}}{R_s} \right) - \frac{R_{\rm gal}}{R_s + R_{\rm gal}} \right].$$

   The resulting relations for $\rho_0 \approx 4 \times 10^7$ $M_\odot$ pc^{-3}, $R_s \approx 130$ kpc, and $\log(r_h/r_J) = -1.0$ are illustrated in Figure 15 as magenta curves and show that even in the presence of a typical dark matter halo, i.e., considering $\mathcal{M}_\star + \mathcal{M}_{\rm DM} = \mathcal{M}_{\rm gal}$ in Equation (9), the r_h–$R_{\rm gal}$ GC relations are still monotonically increasing, albeit not as rapidly as in the case of considering $\mathcal{M}_\star$ only. Hence, an additional component is required to flatten out the r_h–$R_{\rm gal}$ profiles at large galactocentric radii.

2. We therefore suggest that an increased stochastic distribution of low-mass dark matter halos that are part of the galaxy cluster potential induces additional tidal stress on outer-halo GCs. Such a changing mass fraction in subhalos as a function of galactocentric radius is observed in high-resolution ΛCDM simulations (e.g., Springel et al. 2008) and would increase the "tidal variance" in outer-halo regions, thereby truncating the GC stellar density profiles. This may limit the GC sizes to a roughly constant value, something that shall be explored with dedicated high-resolution numerical simulations.

6.2. Structural Parameter Distributions

We show the r_h distribution of NGC 1399 GCs in Figure 16 together with corresponding measurements for Milky Way and M31 GCs, taken from the McMaster catalog (2010 update of Harris 1996) as well as Peacock et al. (2009) and Huxor et al. (2014), respectively. In addition, we compare our half-light radius measurements to the r_h distributions of GCs in NGC 5128 (Woodley & Gómez 2010), the Sombrero galaxy (M104, Harris et al. 2010), and the two brightest Virgo ellipticals, M49 and M87, which were studied by the ACSVCS (for details, see Jordán et al. 2009).

[20] http://cgs.obs.carnegiescience.edu/CGS/Home.html

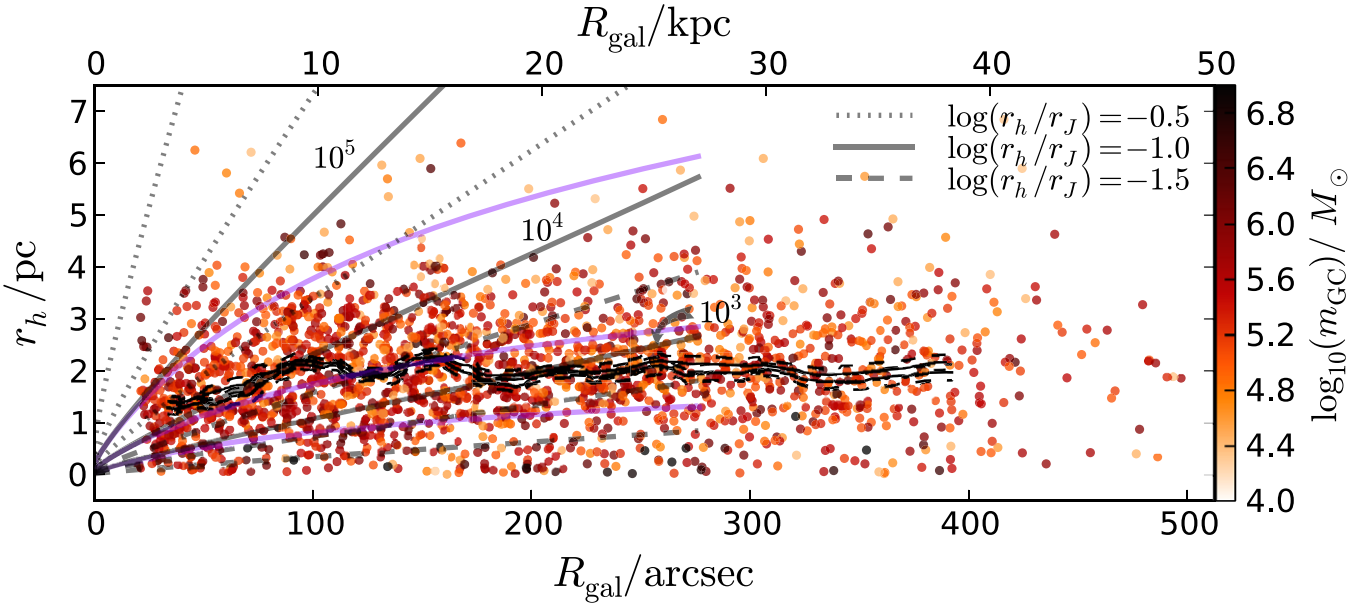

Figure 15. GC half-light radius vs. galactocentric radius as in the top panel of Figure 14. This time we overplot estimates of the GC half-light radius based on the derived GC Jacobi radius for GC masses, $m_{\rm GC} = 10^3$, 10^4, and $10^5\ M_\odot$, and minimum, mean, and maximum ratios between the half-light and Jacobi radii, $\log(r_h/r_J) = -0.5, -1.0, -1.5$, based on the work of Ernst & Just (2013). Gray shaded curves consider only the stellar mass profile of NGC 1399, while magenta curves show the corresponding relations for the combined stellar+dark matter mass density profile (see the text for details).

(A color version of this figure is available in the online journal.)

The bottom panel of Figure 16 shows the entire sample of NGC 1399 GCs together with the distribution of radial-velocity-confirmed GCs (dark histogram) and stars (cyan histogram). It is important to note that all spectroscopically confirmed foreground stars concentrate around $r_h \approx 0$ pc, where unresolved objects are generally expected. We provide mean and median values of each r_h distribution in each panel of Figure 16 and point out that there is a trend of decreasing r_h with increasing host galaxy luminosity (Masters et al. 2010) in which NGC 1399 and its central GC system fit right in. Such a trend generally supports the notion that the host environment has an impact on the GC r_h–$R_{\rm gal}$ relation (see discussion above) and will depend on the sampled $R_{\rm gal}$ range.

We also compare our sample to the measurements of Masters et al. (2010), who derived GC half-light radii for the central regions in NGC 1399 from the ACS Fornax Cluster Survey data (Jordán et al. 2007), which, similar to the ACSVCS in Virgo, sampled massive early-type galaxies in Fornax with one central *HST*/ACS pointing. Both our and the ACSFCS distributions show very similar shapes and drop-offs from ∼1.5 pc up to about 5 pc, beyond which our sample starts to include many more extended GCs. This is mainly due to the nine times larger field of view of our data, and we point out that many of these extended sources are radial-velocity-confirmed bona fide GCs at large galactocentric radii.

The comparison with other GC systems in the upper panels of Figure 16 shows that all half-light radius distributions have very similar shapes featuring a relatively steep increase in GC number density at low r_h values, with a peak somewhere in the range of 2–3 pc and a shallower decline toward more extended objects. This distribution is dependent on the sampling of the GC luminosity function and galactocentric radius, as well as the amount of contamination, the measurement errors, and the GC selection criteria (e.g., Brescia et al. 2012). It is hard to compare the unresolved parts at $r_h \lesssim 1$ pc for galaxies farther away than Sombrero (NGC 4594 at $D \approx 9$ Mpc) because of the resolution limit of *HST* (see shaded regions in Figure 16). Despite this limitation, there is ample information and some intriguing aspects of the GC size distributions for sources with $r_h \gtrsim 1.5$ pc. In NGC 1399, these extended clusters predominantly reside at projected galactocentric radii, $R_{\rm gal}$, larger than 10 kpc (see Figure 14). Since the observed GC populations in M49, M87, and M104 are all inside this radius (see Table 3), we find a very small population of similarly extended GCs in the corresponding samples. This is, of course, an observational bias considering our and the earlier results by van den Bergh et al. (1991) and Larsen & Brodie (2003), who found correlations of the type $r_h \propto R_{\rm gal}^n$ with $n < 1$, and Jordán et al. (2005), who suggested an analytic expression that approximates the r_h distribution for the inner GC systems in Virgo ellipticals.

Having sampled a significant population of GCs to large galactocentric radii in NGC 1399 in combination with similar results for a less rich GC system (see Figure 16), we therefore suggest that all GC systems are composed of two components of clusters: one standard GC population with a size distribution resembling the typical GC half-light radius of 2–3 pc and a second, less rich, component of more extended GCs that are predominantly found at larger galactocentric radii. Alternatively, there might be a combination of mechanisms (explored further below) that act on just one GC population, but their effects manifest themselves at different radii, so that the extended GCs are only observed at large $R_{\rm gal}$.

To quantify the fraction of extended GCs in a GC system, we define the number ratio of GCs with sizes larger than 5 pc relative to the total GC population,

$$E_5 = N_{\rm GC}(r_h \geqslant 5{\rm pc})/N_{\rm GC}({\rm all}), \tag{12}$$

and normalize this value to the Galactic GC system, i.e.,

$$\hat{E}_5 = \frac{N_{\rm GC}(r_h \geqslant 5{\rm pc})}{N_{\rm GC}({\rm all})} \left(\frac{N_{\rm GC}(r_h \geqslant 5{\rm pc})_{\rm MW}}{N_{\rm GC}({\rm all})_{\rm MW}} \right)^{-1}. \tag{13}$$

Table 3
Fractions of Extended GCs for Various GC Systems

Host Galaxy	E_5	$\hat{E}_5$	Ref.	Dist./Mpc	Ref.	R_{gal}/kpc	$E_{5/10}$	$\hat{E}_{5/10}$	$r_e(K_s)$	r_e/kpc	$\mathcal{E}_5$	$\hat{\mathcal{E}}_5$
NGC 1399	0.122	0.62	1	20.13 ± 0.4	7	51.3	0.061	0.21	32.″9	3.21	0.0480	0.12
NGC 4486 (M87)	0.066	0.34	2	16.70 ± 0.2	8	12.3	0.064	0.22	41.″5	3.36	0.0633	0.16
NGC 4472 (M49)	0.073	0.37	2	16.40 ± 0.2	8	11.6	0.072	0.25	56.″1	4.46	0.0714	0.18
NGC 4594 (M104)	0.026	0.13	3	9.08 ± 0.2	9	15	0.024	0.08	55.″3	2.43	0.0160	0.04
NGC 5128 (Cen A)	0.170	0.86	4	3.84 ± 0.35	10	20	0.179	0.61	82.″6	1.54	0.2127	0.54
NGC 224 (M31)	0.241	1.22	5	0.779 ± 0.05	11	160	0.132	0.45	443.″2	1.67	0.1316	0.33
Milky Way	0.197	$\equiv 1$	6	...	...	120	0.292	$\equiv 1$	...	2.50	0.3974	$\equiv 1$

Notes. R_{gal} is the maximum sampling radius of the corresponding data set in kpc. E_5 and $\hat{E}_5$ are the values defined in Equations (12) and (13), while the corresponding values for the GC samples restricted to $R_{gal} \leqslant 10$ kpc are given as $E_{5/10}$ and $\hat{E}_{5/10}$ and those within 2.5 effective radii as $\mathcal{E}_5$ and $\hat{\mathcal{E}}_5$, respectively. K_s-band effective radius measurements, $r_e(K_s)$, are from 2MASS and were obtained from the NASA/IPAC Infrared Science Archive. For the Milky Way, the corresponding value was adopted based on the predictions of the Besançon Galactic stellar population synthesis model (Robin et al. 2003).

References. For the GC populations, (1) this work; (2) ACSVCS, see Jordán et al. (2009); (3) Harris et al. (2010); (4) Woodley & Gómez (2010); (5) Peacock et al. (2009) and Huxor et al. (2014); (6) McMaster catalog, 2010 update of Harris (1996). For the distance measurements; (7) Dunn & Jerjen (2006); (8) Mei et al. (2007); (9) Jensen et al. (2003); (10) Harris et al. (2010); (11) Conn et al. (2012).

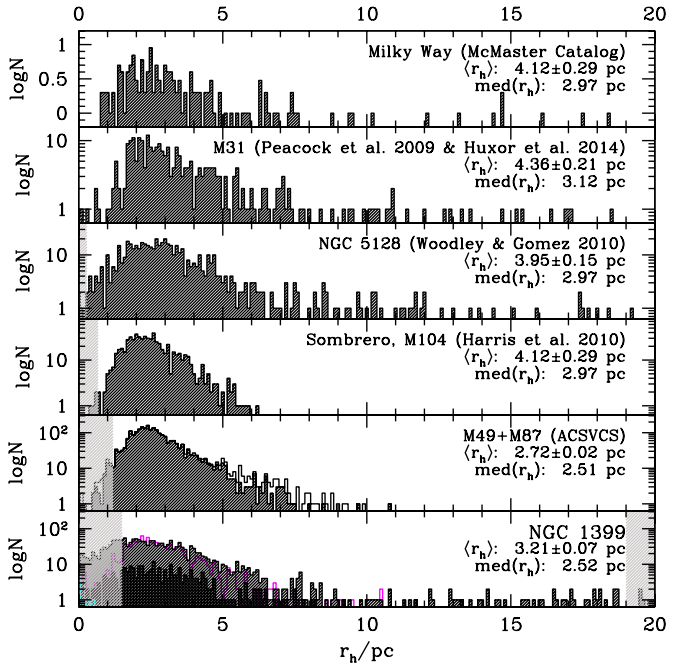

Figure 16. Half-light radius distribution functions for various GC samples. The two top panels show the r_h distributions for the Milky Way and M31 GC system, the measurements of which were taken from the 2010 version of the McMaster catalog (Harris 1996) as well as from Peacock et al. (2009) and Huxor et al. (2014), respectively. The other panels below show the corresponding r_h distributions for GCs in NGC 5128 (Woodley & Gómez 2010), the Sombrero galaxy (M104, Harris et al. 2010), and the two brightest Virgo ellipticals, M49 and M87, studied by the ACSVCS (Jordán et al. 2009). To illustrate the variation in selecting GC photometrically from ACSVCS data, we plot for the two Virgo galaxies the distributions for all objects with a GC likelihood parameter of $p = 0.9$ (likely genuine GCs, shaded histogram) and $p = 0.2$ (GCs and objects that are less likely of GC nature, open histogram; see Jordán et al. for details). The bottom panel shows our r_h measurements for all NGC 1399 GCs as a shaded histogram and for all spectroscopically confirmed GCs as a dark histogram. We also show the distribution of GC half-light radii for the center region of NGC 1399 presented in Masters et al. (2010) based on data from the ACS Fornax Cluster Survey (magenta histogram; see Jordán et al. 2007). Note that all nine confirmed foreground stars are, as expected, unresolved objects (cyan histogram). Assuming observations in the F606W filter, we show the expected resolution limits as gray shaded regions. The gray shaded region in the bottom panel at $r_h \geqslant 19$ pc shows the parameter space section where the correction functions are less robustly defined (see Section 4 for details).

(A color version of this figure is available in the online journal.)

The results for all GC systems are summarized in Table 3 for the galactocentric sampling ranges of the corresponding data set, which vary by about an order of magnitude.

In order to representatively compare the GC samples we therefore restrict each data set to within $R_{gal} \leqslant 10$ kpc (about the maximum homogeneous sampling radius of the samples) as well as 2.5 effective radii of the host galaxy's diffuse light (set by the maximum radial sampling of each data set), measured in the near-infrared K_s filter. We summarize the corresponding values as $E_{5/10}$ and $\hat{E}_{5/10}$ for $R_{gal} \leqslant 10$ kpc as well as $\mathcal{E}_5$ and $\hat{\mathcal{E}}_5$ for $R_{gal} \leqslant 2.5\, r_e$ in Table 3.

We find a clear dichotomy in the $\mathcal{E}_5$ (and $E_{5/10}$) between late-type and early-type galaxies. While the three giant ellipticals NGC 1399, M87, and M49 as well as M104 show $\mathcal{E}_5$ values clearly below 10%, the two late-type spirals, i.e., M31 and the Milky Way, as well as NGC 5128 stand out with significantly higher $\mathcal{E}_5$ values, clearly above ∼10%. We attribute this result to differences in the tidal environment properties throughout the dynamical evolution and merging history of these galaxies. Giant ellipticals experience, in general, a more violent evolution than spirals. It is unclear yet how these numbers compare to other GC systems, but the fact that $\mathcal{E}_5$ values of NGC 1399 and the two Virgo giant ellipticals, M87 and M49, are remarkably similar hints at physical processes that are acting in a similar way on the size evolution of their GC systems. This includes the somewhat surprising result for the Sombrero galaxy's GC system with an $\mathcal{E}_5$ value similar to that of the giant ellipticals. Higher $\mathcal{E}_5$ values for the Milky Way and M31 might be the result of the dynamically more benign tidal field around such distant GCs and/or the younger, i.e., less evolved, nature of NGC 5128, a recent merger remnant, and its GC system. How these numbers will play out for the GC systems in other Virgo cluster galaxies will be shown by the Next Generation Virgo Cluster Survey (NGVS) which achieves a spatial resolution of ∼5 pc for the entire Virgo galaxy cluster out to its virial radius (Ferrarese et al. 2012; Muñoz et al. 2014). At least then it will be clear whether late-type galaxies have a systematically larger population of extended GCs than early-type galaxies, which host GC systems with a relatively smaller population of extended GCs.

Of course, we expect a complex interplay between the formation paths of the compact and extended GCs. In fact, we expect multiple components in the GC size distribution depending on the star cluster formation history and the evolution

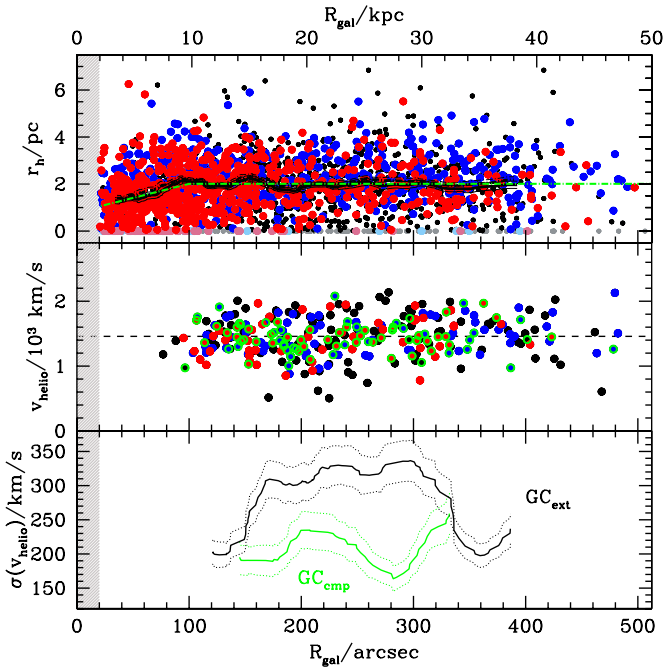

Figure 17. Top panel: all measurements for individual GCs as in Figure 14, with the green dash-dotted curve approximating the running-median relation as defined in Equation (14). We use this empirical separation to define formally compact and extended GCs. Middle panel: The radial velocity of each GC matched with the Schuberth et al. (2010) sample as a function of galactocentric radius. The mean radial velocity of the sample is shown as a horizontal dashed line. The symbols are parameterized by the GC color (see Table 2) and split into blue and red GCs (shown in corresponding colors) and those without color information (shown as black dots). Green circles indicate GCs that have sizes formally more compact than the relation shown as dash-dotted curve in the top panel. Bottom panel: sliding-median relations of the line-of-sight radial velocity dispersion as a function of galactocentric radius for compact (GC_{cmp}, green) and extended (GC_{ext}, black) GCs with their corresponding 90% confidence limits shown as dotted curves.

(A color version of this figure is available in the online journal.)

of the host galaxy. However, in a simplistic picture we speculate that while the primary component GCs (i.e., compact GCs) are likely massive and old and formed in situ, the nature of secondary component GCs (i.e., extended GCs) is likely the result of a combination of populations of (1) dissolving star clusters triggered by recent formation of younger, low-mass GCs combined with increased tidal stress, e.g., in central regions of galaxy clusters or merger remnants (Gieles et al. 2011; Goudfrooij 2012), (2) the accretion of more extended GCs from satellite galaxies that formed and survived in a more benign tidal environment (see also Georgiev et al. 2009a; Da Costa et al. 2009; Smith et al. 2013), and/or (3) disrupting cores of stripped dwarf galaxy nuclei (e.g., Oh & Lin 2000; Bekki & Freeman 2003; Pfeffer & Baumgardt 2013). The corresponding detailed analysis of this scenario is the focus of a forthcoming paper.

6.3. Kinematic Properties of Compact and Extended GCs

The availability of matched GC size and radial velocity measurements in NGC 1399 allows us to investigate correlations between these two parameters. The radial velocities of all GCs with size measurements do not correlate in any statistically significant way as a function of projected galactocentric radius (Figure 17). We measure a total systemic heliocentric radial velocity of the entire sample as $\langle v_{\rm helio}\rangle = 1456 \pm 17$ km s^{-1} with a line-of-sight velocity dispersion of $\sigma = 295$ km s^{-1}, in good agreement with Schuberth et al. (2010). This is also in good agreement and consistent with previous measurements of the diffuse light, i.e., $\langle v_{\rm helio}\rangle = 1425 \pm 4$ km s^{-1} and $\sigma_0 = 353 \pm 19$ km s^{-1} (Graham et al. 1998), respectively.

Next, we divide our sample into populations of compact (GC_{cmp}) and extended (GC_{ext}) GCs using for the division the relation illustrated as the green dash-dotted line in the top panel of Figure 17, which approximates the running-median r_h curve of the entire sample (black curves). This linear separation can be numerically expressed as

$$r_h[\mathrm{pc}] = \begin{cases} 0.012\,R_{\rm gal} + 0.8 & \text{if } R_{\rm gal} < 100'' \\ 2 & \text{if } R_{\rm gal} \geqslant 100''. \end{cases} \quad (14)$$

We scrutinize the GC size–$v_{\rm helio}$ relation for any correlations and find no significant slope for compact and extended GCs as a function of galactocentric radius $R_{\rm gal}$. However, looking at the line-of-sight velocity dispersion, σ, of each of those subsamples, we find a surprisingly clear dichotomy between compact and extended GCs in terms of their mean velocity dispersion. While the compact GC sample exhibits $\langle\sigma_{\rm cmp}\rangle = 225 \pm 25$ km s^{-1}, we compute a much higher value for the extended sample with $\langle\sigma_{\rm ext}\rangle = 317 \pm 21$ km s^{-1}. This is consistent with the σ differences found by Schuberth et al. (2010) between the blue and red GC subpopulations in NGC 1399 at a similar range in galactocentric radius.

Plotting the sliding median of the σ–$R_{\rm gal}$ relation (bottom panel of Figure 17) reveals that this difference is most pronounced in the range $50'' \lesssim R_{\rm gal} \lesssim 320''$, which roughly corresponds to the physical range of $15 \lesssim R_{\rm gal} \lesssim 32$ kpc. Outside this range, the difference seem to disappear, but we lack sample statistics to make definitive conclusions and defer a more detailed analysis of this surprising result to a future study, when more comprehensive radial velocity samples become available. Here we just note that given the scatter of the rather weak correlation between GC size and color (see Section 5.4), the significantly lower velocity dispersion of more compact (i.e., red) GCs compared to their more extended counterparts (i.e., blue GCs) appears to be the astrophysically stronger relation, which likely has its origin in the stronger influence of external tidal truncation effects compared to internal mechanisms that govern the GC size. This is also consistent with our result of the flatter GC size–color relation for the inner versus outer GC sample (see Figure 13). These findings indicate the preferential influence of external dynamical effects damping the size difference between red and blue GCs, which is predominantly driven by the internal evolution of their constituent stellar populations and is likely a corollary of the GC size–dynamics correlation. Future GC radial velocity samples of the inner GC system in NGC 1399 will shed light on how the GC orbit distribution function influences these relations.

Support for *HST* program GO-10129 was provided by NASA through a grant from the Space Telescope Science Institute, which is operated by the Association of Universities for Research in Astronomy, Incorporated, under NASA contract NAS5-26555. This research was supported by FONDECYT Regular Project grant 1121005 and BASAL Center for Astrophysics and Associated Technologies (PFB-06). T.H.P. is thankful for the hospitality and support during his visits at the University of Napoli Federico II, where parts of this work were completed; he also gratefully acknowledges support in the form of a Plaskett Research Fellowship from the National Research Council of Canada. M.P. acknowledges financial support from

the FARO 2011 project of the University of Napoli Federico II. This work was partially supported by the Chandra X-ray Center (CXC), which is operated by the Smithsonian Astrophysical Observatory (SAO) under NASA contract NAS8-03060. We are grateful to Anton Koekemoer and Andy Fruchter for their technical support and useful discussions on the MultiDrizzle code and to Chien Y. Peng for his help with the implementation and testing of the modified GALFIT routine. We thank Tom Richtler and Ylva Schuberth for providing their radial velocity measurements ahead of publication, as well as Luis Ho and Zhao-Yu Li for kindly making available to us their latest NGC 1399 surface brightness profile measurements from the Carnegie–Irvine Galaxy Survey, again prior to publication. Avon Huxor has very kindly supplied M31 GC data prior to publication. We are grateful to the referee, Bill Harris, for providing a thoughtful and constructive report that helped improve the presentation of the results. We thank Jeremy Webb, Mark Gieles, Andres Jordán, Eric Peng, Chunyan Jiang, Stephen Zepf, and Arunav Kundu for valuable discussions and providing data in electronic format. Some of the data presented in this paper were obtained from the Multimission Archive at the Space Telescope Science Institute (MAST). STScI is operated by the Association of Universities for Research in Astronomy, Inc., under NASA contract NAS5-26555. Support for MAST for non-*HST* data is provided by the NASA Office of Space Science via grant NNX09AF08G and by other grants and contracts. This research has made use of the NASA/IPAC Infrared Science Archive, which is operated by the Jet Propulsion Laboratory, California Institute of Technology, under contract with the National Aeronautics and Space Administration. Figures 2 and 3 were created with the help of the ESA/ESO/NASA Photoshop FITS Liberator. This research has made use of NASA's Astrophysics Data System.

Facility: HST(ACS)

REFERENCES

Anderson, J. 2005, in The 2005 HST Calibration Workshop, ed. A. M. Koekemoer, P. Goudfrooij, & L. L. Dressel (Baltimore, MD: Space Telescope Science Institute (STScI))
Anderson, J., & King, I. 2006, Instrument Science Report ACS 2006-001 (Baltimore, MD: STScI), http://www.stsci.edu/hst/acs/documents/isrs/isr0601.pdf
Anderson, J., & King, I. R. 2000, PASP, 112, 1360
Barmby, P., McLaughlin, D. E., Harris, W. E., Harris, G. L. H., & Forbes, D. A. 2007, AJ, 133, 2764
Bassino, L. P., Faifer, F. R., Forte, J. C., et al. 2006, A&A, 451, 789
Bastian, N., Gieles, M., Goodwin, S. P., et al. 2008, MNRAS, 389, 223
Baumgardt, H., & Makino, J. 2003, MNRAS, 340, 227
Baumgardt, H., Parmentier, G., Gieles, M., & Vesperini, E. 2010, MNRAS, 401, 1832
Beckwith, S. V. W., Stiavelli, M., Koekemoer, A. M., et al. 2006, AJ, 132, 1729
Bekki, K. 2010, MNRAS, 401, 2753
Bekki, K., & Freeman, K. C. 2003, MNRAS, 346, L11
Bell, E. F., McIntosh, D. H., Katz, N., & Weinberg, M. D. 2003, ApJS, 149, 289
Bertin, E., & Arnouts, S. 1996, A&AS, 117, 393
Bertin, G., & Varri, A. L. 2008, ApJ, 689, 1005
Binney, J., & Tremaine, S. (ed.) 1987, in Galactic Dynamics (2nd ed.; Princeton, NJ: Princeton Univ. Press), 235
Blakeslee, J. P., Jordán, A., Mei, S., et al. 2009, ApJ, 694, 556
Blom, C., Spitler, L. R., & Forbes, D. A. 2012, MNRAS, 420, 37
Bournaud, F., Duc, P.-A., & Emsellem, E. 2008, MNRAS, 389, L8
Brescia, M., Cavuoti, S., Paolillo, M., Longo, G., & Puzia, T. 2012, MNRAS, 421, 1155
Bruzual, G., & Charlot, S. 2003, MNRAS, 344, 1000
Caon, N., Capaccioli, M., & D'Onofrio, M. 1994, A&AS, 106, 199
Carlson, M. N., & Holtzman, J. A. 2001, PASP, 113, 1522
Chandar, R. 2009, Ap&SS, 324, 315
Chandar, R., Whitmore, B. C., & Fall, S. M. 2010, ApJ, 713, 1343
Chun, M. S., Suh, Y. R., & Lee, Y. B. 1980, JKAS, 13, 27
Conn, A. R., Ibata, R. A., Lewis, G. F., et al. 2012, ApJ, 758, 11
Côté, P., Blakeslee, J. P., Ferrarese, L., et al. 2004, ApJS, 153, 223
Crampton, D., Cowley, A. P., Schade, D., & Chayer, P. 1985, ApJ, 288, 494
Da Costa, G. S. 1979, AJ, 84, 505
Da Costa, G. S., Grebel, E. K., Jerjen, H., Rejkuba, M., & Sharina, M. E. 2009, AJ, 137, 4361
D'Ago, G., Paolillo, M., Fabbiano, G., et al. 2014, A&A, submitted
Demers, S., Grondin, L., & Kunkel, W. E. 1990, PASP, 102, 632
de Vaucouleurs, G., de Vaucouleurs, A., Corwin, H. G., et al. 1991, Third Reference Catalogue of Bright Galaxies (New York: Springer)
Dirsch, B., Richtler, T., Geisler, D., et al. 2003, AJ, 125, 1908
Downing, J. M. B. 2012, MNRAS, 425, 2234
Drinkwater, M. J., Phillipps, S., Jones, J. B., et al. 2000, A&A, 355, 900
Dunn, L. P., & Jerjen, H. 2006, AJ, 132, 1384
Elmegreen, B. G., & Efremov, Y. N. 1997, ApJ, 480, 235
Elmegreen, B. G., & Hunter, D. A. 2010, ApJ, 712, 604
Elson, R., Hut, P., & Inagaki, S. 1987, ARA&A, 25, 565
Elson, R. A., & Walterbos, R. A. M. 1988, ApJ, 333, 594
Elson, R. A. W. 1991, ApJS, 76, 185
Elson, R. A. W. 1992, MNRAS, 256, 515
Elson, R. A. W., Fall, S. M., & Freeman, K. C. 1987, ApJ, 323, 54
Elson, R. A. W., & Freeman, K. C. 1985, ApJ, 288, 521
Elson, R. A. W., & Schade, D. J. 1994, ApJ, 437, 625
Ernst, A., & Just, A. 2013, MNRAS, 429, 2953
Faifer, F. R., Bassino, L. P., Forte, J. C., et al. 2004, BAAA, 47, 132
Fall, S. M., Chandar, R., & Whitmore, B. C. 2009, ApJ, 704, 453
Ferguson, H. C., & Sandage, A. 1989, ApJL, 346, L53
Ferrarese, L., Côté, P., Cuillandre, J.-C., et al. 2012, ApJS, 200, 4
Ford, H. C., Clampin, M., Hartig, G. F., et al. 2003, Proc. SPIE, 4854, 81
Forte, J. C., Faifer, F., & Geisler, D. 2005, MNRAS, 357, 56
Fruchter, A. S., & Hook, R. N. 2002, PASP, 114, 144
Fusi Pecci, F., Battistini, P., Bendinelli, O., et al. 1994, A&A, 284, 349
Georgiev, I. Y., Hilker, M., Puzia, T. H., Goudfrooij, P., & Baumgardt, H. 2009a, MNRAS, 396, 1075
Georgiev, I. Y., Puzia, T. H., Goudfrooij, P., & Hilker, M. 2010, MNRAS, 406, 1967
Georgiev, I. Y., Puzia, T. H., Hilker, M., & Goudfrooij, P. 2009b, MNRAS, 392, 879
Gieles, M., & Bastian, N. 2008, A&A, 482, 165
Gieles, M., Heggie, D. C., & Zhao, H. 2011, MNRAS, 413, 2509
Gnedin, O. Y., & Ostriker, J. P. 1997, ApJ, 474, 223
Gómez, M., Geisler, D., Harris, W. E., et al. 2006, A&A, 447, 877
Gómez, M., & Woodley, K. A. 2007, ApJL, 670, L105
Goudfrooij, P. 2012, ApJ, 750, 140
Graham, A. W., Colless, M. M., Busarello, G., Zaggia, S., & Longo, G. 1998, A&AS, 133, 325
Greif, T. H., Bromm, V., Clark, P. C., et al. 2012, MNRAS, 424, 399
Griffen, B. F., Drinkwater, M. J., Thomas, P. A., & Helly, J. C. 2010, MNRAS, 405, 375
Hack, W., Busko, I., & Jedrzejewski, R. 2003, in ASP Conf. Ser. 295, Astronomical Data Analysis Software and Systems XII, ed. H. E. Payne, R. I. Jedrzejewski, & R. N. Hook (San Francisco, CA: ASP), 453
Harris, G. L. H., Rejkuba, M., & Harris, W. E. 2010, PASA, 27, 457
Harris, W. E. 1996, AJ, 112, 1487
Harris, W. E. 2009, ApJ, 699, 254
Harris, W. E., Harris, G. L. H., & Alessi, M. 2013, ApJ, 772, 82
Harris, W. E., Harris, G. L. H., Barmby, P., McLaughlin, D. E., & Forbes, D. A. 2006, AJ, 132, 2187
Harris, W. E., Harris, G. L. H., Holland, S. T., & McLaughlin, D. E. 2002, AJ, 124, 1435
Harris, W. E., & Pudritz, R. E. 1994, ApJ, 429, 177
Harris, W. E., Spitler, L. R., Forbes, D. A., & Bailin, J. 2010, MNRAS, 401, 1965
Hartwick, F. D. A. 2009, ApJ, 691, 1248
Hénon, M. 1973, A&A, 24, 229
Hénon, M. 1975, in IAU Symp. 69, Dynamics of the Solar Systems, ed. A. Hayli (Dordrecht: Reidel), 133
Hilker, M., Infante, L., Vieira, G., Kissler-Patig, M., & Richtler, T. 1999, A&AS, 134, 75
Ho, L. C., Li, Z.-Y., Barth, A. J., Seigar, M. S., & Peng, C. Y. 2011, ApJS, 197, 21
Huxor, A. P., Tanvir, N. R., Irwin, M. J., et al. 2005, MNRAS, 360, 1007
Huxor, A. P., Mackey, A. D., Ferguson, A. M. N., et al. 2014, MNRAS, in press
Illingworth, G., & Illingworth, W. 1976, ApJS, 30, 227
Innanen, K. A., Harris, W. E., & Webbink, R. F. 1983, AJ, 88, 338
Into, T., & Portinari, L. 2013, MNRAS, 430, 2715
Jee, M. J., Blakeslee, J. P., Sirianni, M., et al. 2007, PASP, 119, 1403

Jensen, J. B., Tonry, J. L., Barris, B. J., et al. 2003, ApJ, 583, 712
Jordán, A. 2004, ApJL, 613, L117
Jordán, A., Blakeslee, J. P., Côté, P., et al. 2007, ApJS, 169, 213
Jordán, A., Côté, P., Blakeslee, J. P., et al. 2005, ApJ, 634, 1002
Jordán, A., Peng, E. W., Blakeslee, J. P., et al. 2009, ApJS, 180, 54
King, I. 1962, AJ, 67, 471
King, I. R. 1966, AJ, 71, 64
King, I. R., Hedemann, E. J., Hodge, S. M., & White, R. E. 1968, AJ, 73, 456
Koekemoer, A. M., Fruchter, A. S., Hook, R. N., & Hack, W. 2003, in The 2002 HST Calibration Workshop, ed. S. Arribas, A. Koekemoer, & B. Whitmore (Baltimore, MD: Space Telescope Science Institute (STScI)), 337
Kontizas, M., Danezis, E., & Kontizas, E. 1982, A&AS, 49, 1
Kotulla, R., Fritze, U., Weilbacher, P., & Anders, P. 2009, MNRAS, 396, 462
Kozhurina-Platais, V., Goudfrooij, P., & Puzia, T. H. 2007, Instrument Science Report ACS 2007-04 (Baltimore, MD: STScI), www.stsci.edu/hst/acs/documents/isrs/isr0704.pdf
Kravtsov, A. V., & Gnedin, O. Y. 2005, ApJ, 623, 650
Kron, R. G. 1980, ApJS, 43, 305
Kukarkin, B. V., & Kireeva, N. N. 1979, SvA, 23, 261
Kundu, A. 2008, AJ, 136, 1013
Kundu, A., & Whitmore, B. C. 1998, AJ, 116, 2841
Kundu, A., & Whitmore, B. C. 2001, AJ, 121, 2950
Kundu, A., Whitmore, B. C., Sparks, W. B., et al. 1999, ApJ, 513, 733
Larsen, S. S. 1999, A&AS, 139, 393
Larsen, S. S., & Brodie, J. P. 2003, ApJ, 593, 340
Larsen, S. S., Brodie, J. P., Huchra, J. P., Forbes, D. A., & Grillmair, C. J. 2001, AJ, 121, 2974
Li, Y., Mac Low, M.-M., & Klessen, R. S. 2005, ApJ, 626, 823
Li, Z.-Y., Ho, L. C., Barth, A. J., & Peng, C. Y. 2011, ApJS, 197, 22
Lotz, J. M., Telford, R., Ferguson, H. C., et al. 2001, ApJ, 552, 572
Madrid, J. P., Harris, W. E., Blakeslee, J. P., & Gómez, M. 2009, ApJ, 705, 237
Mapelli, M., & Bressan, A. 2013, MNRAS, 430, 3120
Maraston, C. 2005, MNRAS, 362, 799
Marín-Franch, A., Aparicio, A., Piotto, G., et al. 2009, ApJ, 694, 1498
Masters, K. L., Jordán, A., Côté, P., et al. 2010, ApJ, 715, 1419
McLaughlin, D. E., Barmby, P., Harris, W. E., Forbes, D. A., & Harris, G. L. H. 2008, MNRAS, 384, 563
McLaughlin, D. E., & van der Marel, R. P. 2005, ApJS, 161, 304
Mei, S., Blakeslee, J. P., Côté, P., et al. 2007, ApJ, 655, 144
Misgeld, I., & Hilker, M. 2011, MNRAS, 414, 3699
Misgeld, I., Hilker, M., & Mieske, S. 2011, in EAS Publication Series, Vol. 48, CRAL-2010 A Universe of Dwarf Galaxies, ed. M. Koleva, Ph. Pruanie, & I. Vanglin (Cambridge: Camrbidge Univ. Press), 207
Monet, D. G., Levine, S. E., Canzian, B., et al. 2003, AJ, 125, 984
Muñoz, R. P., Puzia, T. H., Lançon, A., et al. 2014, ApJS, 210, 4
Murphy, B. W., Cohn, H. N., & Hut, P. 1990, MNRAS, 245, 335
Murray, N. 2009, ApJ, 691, 946
Murray, S. D., & Lin, D. N. C. 1992, ApJ, 400, 265
Navarro, J. F., Frenk, C. S., & White, S. D. M. 1996, ApJ, 462, 563
Oh, K. S., & Lin, D. N. C. 2000, ApJ, 543, 620
Paolillo, M., Puzia, T. H., Goudfrooij, P., et al. 2011, ApJ, 736, 90
Peacock, M. B., Maccarone, T. J., Waters, C. Z., et al. 2009, MNRAS, 392, L55
Peng, C. Y., Ho, L. C., Impey, C. D., & Rix, H.-W. 2010, AJ, 139, 2097
Peng, E. W., Jordán, A., Blakeslee, J. P., et al. 2009, ApJ, 703, 42
Peng, E. W., Jordán, A., Côté, P., et al. 2006, ApJ, 639, 95
Pfeffer, J., & Baumgardt, H. 2013, MNRAS, 433, 1997
Puzia, T. H., Kissler-Patig, M., Brodie, J. P., & Huchra, J. P. 1999, AJ, 118, 2734
Puzia, T. H., Kissler-Patig, M., Brodie, J. P., & Schroder, L. L. 2000, AJ, 120, 777
Puzia, T. H., Zepf, S. E., Kissler-Patig, M., et al. 2002, A&A, 391, 453
Renaud, F., Gieles, M., & Boily, C. M. 2011, MNRAS, 418, 759
Rhode, K. L., & Zepf, S. E. 2001, AJ, 121, 210
Rhode, K. L., & Zepf, S. E. 2004, AJ, 127, 302
Rhode, K. L., Zepf, S. E., Kundu, A., & Larner, A. N. 2007, AJ, 134, 1403
Rhodes, J. D., Massey, R. J., Albert, J., et al. 2007, ApJS, 172, 203
Richtler, T. 2003, LNP, 635, 281
Riess, A., & Mack, J. 2004, Instrument Science Report ACS 2004-006 (Baltimore, MD: STScI), also available at http://www.stsci.edu/hst/acs/documents/isrs/isr0406.pdf
Robin, A. C., Reylé, C., Derrière, S., & Picaud, S. 2003, A&A, 409, 523
Sandage, A. 1975, ApJ, 202, 563
Schlafly, E. F., & Finkbeiner, D. P. 2011, ApJ, 737, 103
Schlegel, D. J., Finkbeiner, D. P., & Davis, M. 1998, ApJ, 500, 525
Schuberth, Y., Richtler, T., Hilker, M., et al. 2010, A&A, 513, A52
Schulman, R. D., Glebbeek, V., & Sills, A. 2012, MNRAS, 420, 651
Sersic, J. L. 1968, Atlas de Galaxias Australes (Cordoba: Observatorio Astronomico)
Sharina, M. E., Puzia, T. H., & Makarov, D. I. 2005, A&A, 442, 85
Sippel, A. C., Hurley, J. R., Madrid, J. P., & Harris, W. E. 2012, MNRAS, 427, 167
Sirianni, M., et al. 2005, PASP, 117, 1049
Smith, R., Sánchez-Janssen, R., Fellhauer, M., et al. 2013, MNRAS, 429, 1066
Spitler, L. R., Larsen, S. S., Strader, J., et al. 2006, AJ, 132, 1593
Springel, V., Wang, J., Vogelsberger, M., et al. 2008, MNRAS, 391, 1685
Taylor, M. A., Puzia, T. H., Harris, G. L., et al. 2010, ApJ, 712, 1191
Trager, S. C., King, I. R., & Djorgovski, S. 1995, AJ, 109, 218
Usher, C., Forbes, D. A., Spitler, L. R., et al. 2013, MNRAS, 436, 1172
van den Bergh, S., Morbey, C., & Pazder, J. 1991, ApJ, 375, 594
Vesperini, E., & Heggie, D. C. 1997, MNRAS, 289, 898
Vesperini, E., & Zepf, S. E. 2003, ApJL, 587, L97
Webb, J. J., Harris, W. E., & Sills, A. 2012a, ApJL, 759, L39
Webb, J. J., Harris, W. E., Sills, A., & Hurley, J. R. 2013, ApJ, 764, 124
Webb, J. J., Sills, A., & Harris, W. E. 2012b, ApJ, 746, 93
Wilson, C. P. 1975, AJ, 80, 175
Woodley, K. A., & Gómez, M. 2010, PASA, 27, 379
Zepf, S. E., Ashman, K. M., English, J., Freeman, K. C., & Sharples, R. M. 1999, AJ, 118, 752
Zibetti, S., Charlot, S., & Rix, H.-W. 2009, MNRAS, 400, 1181